INL/EXT-15-36683

Light Water Reactor Sustainability Program

Monitoring, Modeling, and Diagnosis of Alkali-Silica Reaction in Small Concrete Samples

September 2015

U.S. Department of Energy

Office of Nuclear Energy

INL/EXT-15-36683
Revision 0

Monitoring, Modeling, and Diagnosis of Alkali-Silica Reaction in Small Concrete Samples

Vivek Agarwal[1], Guowei Cai[2], Andrei V. Gribok[1], Paromita Nath[2], Reagan Hansley[2], Kyle Neal[2], Yanqing Bao[2], and Sankaran Mahadevan[2]

September 2015

[1]Idaho National Laboratory
Idaho Falls, Idaho 83415
http://www.inl.gov

[2]Vanderbilt University, Civil and Environmental Engineering
Nashville, Tennessee 37235

Prepared for the
U.S. Department of Energy
Office of Nuclear Energy
Under DOE Idaho Operations Office
Contract DE-AC07-05ID14517

(This page intentionally left blank)

ABSTRACT

Assessment and management of aging concrete structures in nuclear power plants require a more systematic approach than simple reliance on existing safety code margins. Structural health monitoring of concrete structures aims to understand the current health condition of a structure based on heterogeneous measurements to produce high-confidence actionable information regarding structural integrity that supports operational and maintenance decisions.

This report describes alkali-silica reaction (ASR) degradation mechanisms and factors influencing ASR. A fully coupled thermo-hydro-mechanical-chemical model (developed by Saouma and Perotti, 2006) that considers the effects of stress on the reaction kinetics and anisotropic volumetric expansion is presented in this report. This model is implemented in the GRIZZLY code based on the Multiphysics Object-Oriented Simulation Environment. The implemented model in the GRIZZLY code is randomly used to initiate ASR in a two- and three-dimensional lattice to study the percolation aspects of concrete. The percolation aspects help determine the transport properties of the material and the durability and service life of concrete.

This report summarizes the effort to develop small-sized concrete samples with embedded glass to mimic ASR. The concrete samples were treated in water and sodium hydroxide solution at an elevated temperature to study how ingress of sodium ions and hydroxide ions impact concrete samples embedded with glass. A thermal camera was used to monitor the changes in the concrete samples and the subsequent results are summarized in this report.

(This page intentionally left blank)

EXECUTIVE SUMMARY

One challenge for the current fleet of light water reactors in the United States (U.S.) is age-related degradation of their passive assets that include concrete, cables, piping, and reactor pressure vessel. As the current fleet of nuclear power plants (NPPs) continue to operate up to 60 years or beyond, it is important to understand the current and the future health condition of passive assets under different operating conditions that would support operational and maintenance decisions. To ensure long-term safe and reliable operation of the current fleet, the U.S. Department of Energy's Office of Nuclear Energy funds the Light Water Reactor Sustainability (LWRS) Program to develop the scientific basis for extending the operation of commercial light water reactors beyond the current license extension period. The LWRS Program has three pathways. The online monitoring research of assets in nuclear power plants is within the scope of research activities performed within the advanced instrumentation, information, and control systems technologies pathway. This effort also leverages the research performed within the material aging and degradation pathway.

Among different passive assets of interest, concrete structures are investigated in this research project. Reinforced concrete structures found in NPPs can be grouped into four categories: primary containment, containment internal structures, secondary containments/reactor buildings, and spent fuel pool and cooling towers. These concrete structures are affected by a variety of degradation mechanisms, related to chemical, physical, and mechanical causes, and irradiation. The age-related degradation of concrete results in gradual microstructural changes (slow hydration, crystallization of amorphous constituents, reactions between cement paste and aggregates, etc.). Changes over long periods of time must be measured, monitored, and analyzed to best support long-term operation and maintenance decisions.

Structural health monitoring (SHM) of concrete structures aims to understand the current health condition of a structure based on heterogeneous measurements to produce high-confidence actionable information regarding structural integrity and reliability. To achieve this research objective, Vanderbilt University, in collaboration with Idaho National Laboratory (INL) and Oak Ridge National Laboratory has proposed a probabilistic framework of research activities for the health monitoring of NPP concrete structures subject to physical, chemical, and mechanical degradation. A systematic approach proposed to assess and manage aging concrete structures requires an integrated framework that includes the following four elements: damage modeling, monitoring, data analytics, and uncertainty quantification.

After proposing the above framework, INL and Vanderbilt University demonstrated through a simple concrete sample each element of the proposed probabilistic SHM framework. The research was focused on concrete SHM measurements, data analytics, and development of uncertainty-quantified diagnostic and prognostics models that will support continuous assessment of concrete performance. In this ongoing effort, the focus is to understand the alkali-silica reaction (ASR) in a concrete structure. ASR is a chemical reaction between the alkali hydroxides (Na, K, and OH) from the cement and unstable silica (silicon dioxide) in some type of aggregate. The reaction produces an alkali-silica gel that expands internally by absorbing water from the surrounding paste and eventually leading to cracking of the surrounding concrete. This degradation is intrinsic and extremely difficult to detect.

To develop suitable instrumentation/monitoring techniques to detect ASR, it is important to theoretically understand its development mechanism in presence of different influencing factors. Therefore, in this phase of the research, mathematical model developed by Saouma and Perotti (2006) is used to understand ASR expansion. Saouma and Perotti (2006) developed a fully coupled thermo-hydro-mechanical-chemical for ASR based on Ulm et al. (2000) model, and considered the effects of stress on the reaction kinetics and anisotropic volumetric expansion induced by gel. The model was implemented in the GRIZZLY code based on the Multiphysics Object-Oriented Simulation Environment framework. These experimental measurements are used to validate the anisotropic ASR swelling model implemented in GRIZZLY. The simulation of ASR expansion using GRIZZLY code provided essential insight on the

volumetric expansion mechanism and would lay the foundation for development of monitoring techniques.

The implemented model in the GRIZZLY code is randomly used to initiate ASR in a two- and three-dimensional lattice to study the percolation aspects of concrete. Percolation theory plays an important role in interpreting and understanding the microstructure of cement-based material. The percolation aspects help determine the transport properties of the material and therefore the durability and service life of concrete. These transport properties are function of percolation threshold.

In a parallel activity, Vanderbilt University developed small sized concrete samples with embedded glass (basically silica), which has a strong ability to form ASR and provides a quick proof-of-concept for the proposed SHM framework. The silica in glass reacts with the calcium in cement to form calcium silicate hydride (ASR gel) in the presence of sodium hydroxide. Two sets of three samples each sized 9 in. × 5 in. × 2 in. were cast. For better test sample control, aggregates were replaced by glass (approximately 75% silicon dioxide) in these experiments. By performing data analysis of thermal images, the deformation of glass under thermal loading profile was studied.

In the next phase of the research, Vanderbilt University in collaboration with Professor Eric Giannini of University of Alabama will be working on developing medium sized concrete samples (2 ft × 2 ft × 6 in.) using reactive aggregates with and without steel reinforcement. Full field imaging techniques will be applied to detect ASR expansion in the medium sized sample. A strong theoretical basis will be established and validated to support the proposed monitoring techniques. A data analytics and visualization framework will be developed to analyze and visualize heterogeneous data on a unified and easy-to-use visualization platform. Diagnostic uncertainty quantification will also be formed.

In fiscal year 2016, a collaborative research effort will be performed between the Advanced Instrumentation, Information, and Control and Material Aging and Degradation pathways under the LWRS Program to support large concrete sample instrumentation, data analysis, and uncertainty quantification elements of the SHM framework.

ACKNOWLEDGMENTS

This report was made possible through funding by the U.S. Department of Energy (DOE) Light Water Reactor Sustainability Program. We are grateful to Richard Reister of DOE, and Bruce Hallbert and Kathryn McCarthy at Idaho National Laboratory for championing this effort. We thank Jodi L. Vollmer for her technical editing and formatting of the document. We also thank Benjamin W. Spencer and Hai Huang at Idaho National Laboratory for providing access to the GRIZZLY code and for their technical guidance on code implementation.

(This page intentionally left blank)

CONTENTS

FIGURES

TABLES

(This page intentionally left blank)

ACRONYMS

ASR	alkali-silica reaction
BN	Bayesian network
INL	Idaho National Laboratory
LWRS	Light Water Reactor Sustainability
MOOSE	Multiphysics Object-Oriented Simulation Environment
NPP	nuclear power plant
ORNL	Oak Ridge National Laboratory
SHM	structural health monitoring
SMA	simple moving average
U.S.	United States

(This page intentionally left blank)

1. INTRODUCTION

As many existing nuclear power plants (NPPs) continue to operate beyond their licensed life cycle, plant structures, systems, and components suffer deterioration that affects NPP structural integrity and performance. Health monitoring is an essential technology for ensuring that the current and future state of a NPP will meet performance and safety requirements. This project focuses on concrete structures in NPPs. The concrete structures are grouped into four categories (1) primary containment, (2) containment internal structures, (3) secondary containment/reactor buildings, and (4) other structures such as used fuel pools, dry storage casks, and cooling towers. These concrete structures are affected by a variety of chemical, physical, and mechanical degradation mechanisms such as alkali-silica reaction (ASR), chloride penetration, sulfate attack, carbonation, freeze-thaw cycles, shrinkage, and mechanical loading (Naus 2007). The age-related deterioration of concrete results in continuing microstructural changes (i.e., slow hydration, crystallization of amorphous constituents, reactions between cement paste and aggregates, etc.). Therefore, it is important that changes over long periods of time are measured, monitored, and analyzed to best support long-term operation and maintenance decisions.

Structural health monitoring (SHM) is required to produce actionable information regarding structural integrity that when conveyed to the decision-maker will enable risk management in regards to structural integrity and performance. The methods and technologies employed include the assessment of the critical measurements, monitoring, and the analysis of aging concrete structures under different operating conditions. In addition to the specific system being monitored, information may also be available for similar or nominally identical systems in a fleet, as well as legacy systems. Therefore, Christensen (1990) suggested that assessment and management of the aging concrete structures in NPPs require a more systematic approach than simple reliance on existing code margins of safety.

Through the Light Water Reactor Sustainability (LWRS) Program, several national laboratories, and Vanderbilt University have started the concrete SHM research and development per the proposed framework discussed in the following section. The research goal is to enable plant operators to make risk-informed decisions on structural integrity, remaining useful life, and performance of concrete structures across the nuclear fleet. The long-term research objective of this project is to produce actionable information regarding structural integrity that supports operational and maintenance decision making, which is individualized for a given structure and its performance goals. In addition, the project supports the research objectives of all three pathways under the LWRS Program.

This report presents a discussion on fully coupled thermo-hydro-mechanical-chemical model developed by Saouma and Perotti (2006) by taking into consideration the effects of stress on the reaction kinetics and anisotropic volumetric expansion due to ASR. This model is implemented in the GRIZZLY code based on the Multiphysics Object-Oriented Simulation Environment (MOOSE). The implemented model in the GRIZZLY code is randomly used to initiate ASR in a two- and three-dimensional lattice to study the percolation aspects of concrete. The percolation aspects help determine the material transport properties and the concrete durability and service life. This report also summarizes the effort to develop small-sized concrete samples with embedded glass to mimic ASR. The concrete samples were treated in water and sodium hydroxide (NaOH) solution at an elevated temperature to study how ingress of sodium ions and hydroxide ions impact concrete samples embedded with glass. A thermal camera was used to monitor the changes in the concrete sample and results are summarized.

1.1 Background

Vanderbilt University, in collaboration with Idaho National Laboratory (INL) and Oak Ridge National Laboratory (ORNL) personnel, proposed a framework for health diagnosis and prognosis of aging concrete structures in NPPs subject to physical, chemical, and mechanical degradation (Mahadevan et al. 2014, Agarwal and Mahadevan 2014). The proposed framework (shown in Figure 1) will investigate the health of NPP concrete structures by integrating four technical elements: (1) damage

modeling, (2) monitoring, (3) data analytics, and (4) uncertainty quantification. For details on the application of each element of the proposed framework on a small concrete sample, refer Mahadevan et al. (2015). The framework will enable plant operators to make risk-informed decisions on the structural integrity, remaining useful life, and performance of concrete structures.

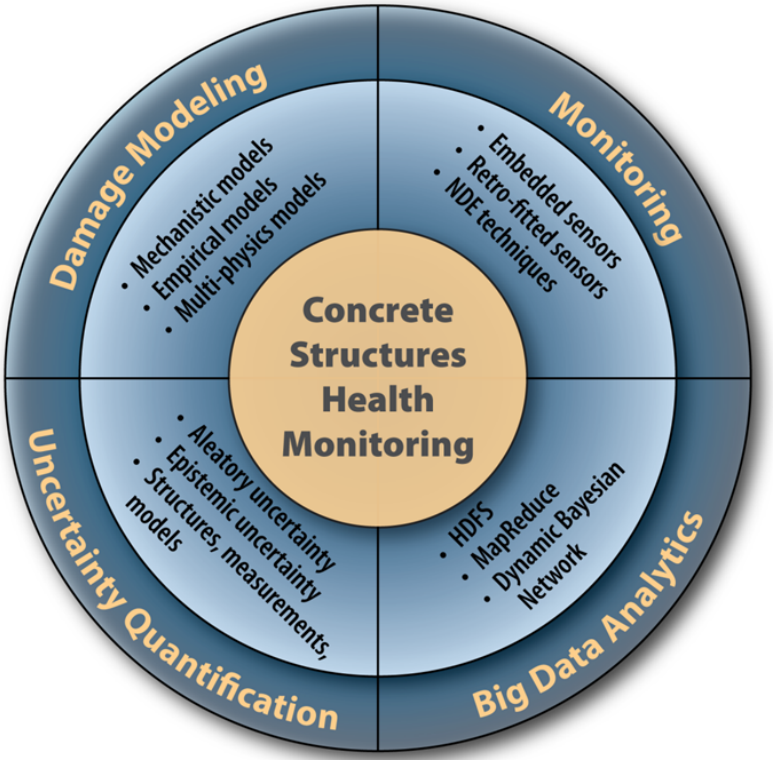

Figure 1. Elements of concrete structural health monitoring.

Damage Modeling: This element leverages the modeling of chemical, physical, and mechanical degradation (i.e., alkali-aggregate reaction, chloride penetration, sulfate attack, carbonation, freeze-thaw cycles, shrinkage, and radiation damage) to assist monitoring and risk management decisions. Alkali-aggregate reaction is currently receiving prominent attention; however, other appropriate damage mechanisms for NPP concrete structures can also be included. The interactions of multiple mechanisms need significant consideration. The task requires modeling and computational advances, combined-physics experiments, and the integration of multiple models through an appropriate simulation framework.

Monitoring: This element explores effective combination of promising SHM techniques for full-field multiphysics monitoring of concrete structures. Optical, thermal, acoustic, and radiation-based techniques will be investigated for full-field imaging. Examples of these techniques include digital image correlation, infrared imaging, velocimetry and ultrasonic, and X-ray tomography. A particular consideration is the linkage of chemical degradation mechanisms to the observed degradation, which requires synergy between the damage modeling and monitoring research.

Data Analytics: The information gathered from multiple health monitoring techniques results in high volume, rate, and variety (heterogeneity) of data. This element leverages big data techniques to store, process, and analyze heterogeneous data (numerical, text, and image) and arrive at effective inference of concrete degradation. The data analytics framework can also integrate information from model prediction, laboratory experiments, plant experience and inspections, and expert opinion. Data mining, classification

and clustering, feature extraction and selection, and fault signature analyses with heterogeneous data can be orchestrated through a Bayesian network (BN) for effective inference

Uncertainty Quantification: This element will quantify the uncertainty in health diagnosis and prognosis in a manner that facilitates risk-management decisions. Sources of natural variability, data uncertainty and model uncertainty arising in both modeling and monitoring activities can be considered and their effects quantified. In addition to measurement and processing errors, data uncertainty from sparse and imprecise data for some quantities, and large data on other quantities (data quality, relevance, scrubbing) can be considered. Model uncertainty in multiphysics degradation modeling due to model form, model parameters, and solution approximations can be included. The various uncertainty sources do not combine in a simple manner; therefore, a systematic BN approach should be developed for comprehensive uncertainty quantification in a manner that is informative to the decision-maker for operation, maintenance, inspection, and other risk-management activities.

As part of the ongoing research effort, a fully coupled thermo-hydro-mechanical-chemical model for ASR developed by Saouma and Perotti (2006) was implemented in the GRIZZLY code of the MOOSE framework. The model is based on Ulm et al. (2000) model, and considers the effects of stress on the reaction kinetics and anisotropic volumetric expansion induced by gel. The ASR model in GRIZZLY was to study the percolation aspects of concrete. The percolation aspects help determine the transport properties of the material and therefore the durability and service life of concrete. These transport properties are function of percolation threshold.

In a parallel activity, Vanderbilt University developed small sized concrete samples with embedded glass (which is basically silica [Si]) that has a strong ability to form ASR and provide a quick proof-of-concept for the proposed SHM framework. Data analysis of thermal images is performed to study deformation of glass embedded in concrete sample under thermal loading profile.

1.2 Report Layout

The objective of this report is to present research efforts in the direction of modeling, monitoring, and concrete sample development. The report is organized as follows:

- Section 2 discusses the mechanism of ASR in concrete structures.
- Section 3 presents the implementation of a fully coupled thermo-hydro-mechanical-chemical model developed by Saouma and Perotti (2006) that evaluates the effects of stress on the reaction kinetics and anisotropic volumetric expansion in the GRIZZLY code based on the MOOSE.
- Section 4 presents a percolation aspects study performed on a two- and three-dimensional lattice using randomly generated ASR initiation in GRIZZLY.
- Section 5 talks about small-sized concrete sample development with embedded glass and the application of thermal imaging in detecting the formation of glass gel (mimicking ASR gel) in presence of NaOH.
- Section 6 discusses the research summary and future activities.

2. ALKALI-SILICA REACTION IN CONCRETE STRUCTURES

Aggregates containing certain constituents can react with alkali hydroxides in concrete. The reactivity is potentially harmful only when it produces significant expansion (Mather 1975). This alkali-aggregate reactivity has two forms—ASR and alkali-carbonate reaction (sometimes called alkali-carbonate rock reaction). ASR is more often a concern than alkali-carbonate reaction because the occurrence of aggregates containing reactive silica minerals is more common. Alkali-silica reactivity has been recognized as a potential source of distress in concrete since the late 1930s (Stanton 1940 and PCA 1940).

Reducing ASR potential requires an understanding of the ASR mechanism, properly using tests to identify potentially reactive aggregates, and if needed, taking steps to minimize the potential for expansion and related cracking.

2.1 Mechanism of Alkali-Silica Reaction

Concrete consists of aggregates—stone or gravel and sand, in a matrix of cement paste. The cement paste contains interconnected microscopic pores through which water or ions in solution can migrate. The ASR forms a gel that swells as it draws water from the surrounding cement paste. Reaction products from ASR have a great affinity for moisture (i.e., hygroscopic). In absorbing water, these gels can induce pressure, expansion, and cracking of the aggregate and surrounding paste. The reaction can be expressed as a two-step process and can be visualized as shown in Figure 2.

1. Alkali + reactive silica → alkali-silica gel
2. Alkali-silica gel + moisture → expansion.

It is precisely the second reaction that causes the well-known swelling of the concrete, resulting in major internal stress redistribution inside the concrete structures that manifests itself either through large compressive stresses, and/or more dramatically through the formation of structural cracks or the sliding across the critical joints. Hence, the structural integrity of the structure can certainly be seriously jeopardized by the pernicious and slow evolution of the reaction.

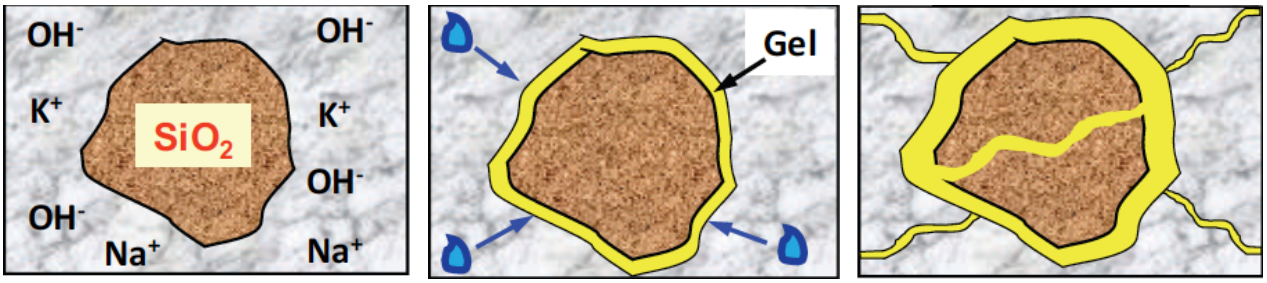

(a) (b) (c)

Figure 2. Sequence of ASR (Thomas et al. 2011). (a) Reaction between the alkali hydroxides (Na, K, and OH) from the cement and unstable silica (SiO_2) in some type of aggregate; (b) the reaction produces an alkali-silica gel that expands by absorbing water from the surrounding paste; and (c) the gel expands internally and eventually leads to cracking of the surrounding concrete.

However, the presence of gel does not necessarily indicate destructive ASR. Some gels expand very little or not at all. If a gel is low swelling, it will not create problems. High-swelling gel may cause pressures exceeding the concrete tensile strength, which results in concrete cracking. The rate of pore fluid migration to the reaction site and temperature also influence swelling pressures (Diamond, Barneyback, and Struble 1981). Consequently, the presence of gel must be linked to destructive cracking for a positive identification of harmfully expansive ASR.

2.2 Factors Affecting Alkali-Silica Reaction

For ASR to occur, three conditions must be present:

- Reactive form of silica in the aggregate
- High-alkali (pH) pore solution
- Sufficient moisture.

The amount of gel formed in the concrete depends on the amount and type of reactive silica, and the alkali hydroxide concentration in the concrete pore solution. Natural aggregates contain various forms of silica minerals, which have varying reactivities—measures of the readiness of the silica to react with alkali. Internal sources of alkali (sodium and potassium) can come from the cement, pozzolans, aggregates, and mixtures, and mix water. When the alkali and silica react, they form the gel reaction product. External alkalies can come from a number of sources, but the predominant source is anti-icing or deicing chemicals. Exact composition will vary, but the gel always contains alkali, calcium, silica, and water (Xu 1987).

Reactive silica in the aggregate. Reactivity is a function of the type and form of constituents composing the aggregate. The constituent minerals of an aggregate are obtained from a petrographic analysis. The following rock types contain critical amounts of potentially reactive forms of silica: chert and flint containing chalcedony; acidic and intermediate volcanic rocks, such as rhyolite, dacite, latite, and andesite, and the associated porphyries and tuffs; shale and slate; sandstone, siltstone, and quartzite; siliceous carbonate rocks; graywackes; argillites; phyllites; granites and grano-diorites; granite and grano-diorite gneisses. The list is not all-inclusive, and many aggregates listed will perform adequately in concrete that contains more than enough alkali to promote ASR. Fine and coarse aggregate containing more than the following quantities of constituents are considered potentially reactive (adapted from NRMCA 1993):

- Opal—more than 0.5% by mass
- Chert or chalcedony—more than 3.0%
- Tridymite or cristobalite—more than 1.0%
- Optically strained or microcrystalline quartz— more than 5.0% (as found in granites, granite gneiss, graywackes, argillites, phyllites, siltstones, and some natural sands and gravels)
- Natural volcanic glasses—more than 3.0%.

High-alkali-content pore solution. Alkali hydroxides in solution will react readily with reactive forms of silica in aggregate. As the aggregate reactivity increases, gel reaction products can be formed with lesser concentrations of alkali. That is why the use of low-alkali cements alone may not be sufficient to control ASR with highly reactive aggregates.

As the pH (or alkalinity) of the pore solution increases, potential for the alkali-silica reaction increases. At higher concentrations of alkali hydroxides, even the more stable forms of silica are susceptible to attack (Xu 1987). If the alkali concentration is great enough, the alkali hydroxides break stronger silicon bonds found in less reactive aggregates to form the gel reaction product. This explains why aggregates thought to be nonreactive sometimes exhibit ASR.

Repeated cycles of wetting and drying can create high-localized concentrations of alkalies. As moisture travels through concrete, dissolved alkalies move in solution, remaining when the moisture evaporates from the concrete surface. This process, known as alkali migration, can cause high alkali concentrations at an evaporative surface even when the overall concrete alkali content is low.

Sufficient moisture. Moisture allows migration of alkali ions to reaction sites and the resulting gel

absorbs moisture, leading to expansion. For this reason, deleterious ASR does not occur in concretes that are dry in service. Research has shown that expansive ASR can occur in concrete having a relative humidity above 80% (Stark 1991). However, it is possible for well-cured concrete in arid regions to have a relative humidity constantly at or above 80% just beneath its surface, even after several decades. Any reduction in permeability, by using a low water-cement ratio, supplementary cementitious materials, or other means, reduces movement of moisture and alkalies into and within the concrete.

Concrete alkali content. The potential for ASR increases as the alkali content of concrete increases. In the U.S., the method often used to control the concrete alkali content is to specify low-alkali cement (defined in ASTM C 150 of AASHTO M 85) as having an equivalent sodium oxide content of no more than 0.60%. However, concrete made with low-alkali cement can still exhibit expansive ASR if moisture movement concentrates the alkalies in one location (Perenchio, Kaufman, and Krause 1991); if the aggregate is extremely reactive; if alkalies are provided by certain supplementary cementitious materials and chemical admixtures, as well as from the aggregates and mixing water; or if total alkali content of concrete is high due to a high cement content. Alkalies from external sources can also contribute significantly to the concrete alkali content. External alkalies may increase expansion from ASR, especially when concrete is cracked or is highly permeable. Common sources of external alkalies are deicing salts, seawater, groundwater, and water from industrial processes. In particular, use of pavement deicers can contribute significantly to alkalies.

There are ways to reduce the ingress of external alkalies. In addition to proper handling, placing, and curing of concrete, the use of supplementary cementitious materials and a low water-cementitious materials ratio will reduce concrete permeability, slow the entrance of external alkalies, and reduce potential ASR expansion. Protective coatings and sealers provide a barrier to seawater, deicing salts, and other alkali sources.

Temperature. Structures in warmer exposures are more susceptible to ASR than those in colder exposures because the ASR rate usually increases with increasing temperature (Perenchio, Kaufman, and Krause 1991). For the majority of aggregates, higher temperatures also mean larger ultimate expansions. However, there are studies showing that lower temperatures, 13°C and 20°C (55°F and 68°F) compared to 38°C (100°F), resulted in significantly larger ultimate expansions with certain aggregates (Jones and Poole 1987). The effect of high or low temperatures on ultimate expansion is aggregate dependent with most aggregates reacting more at higher temperatures.

2.3 Alkali-Silica Reaction Expansion

Typical indicators of ASR presence are longitudinal cracking, map (random pattern) cracking, and in advanced cases, closed joints, spalled concrete surfaces, or relative displacements of different portions of a structure. Because ASR deterioration is slow, the risk of catastrophic failure is low. ASR can cause serviceability problems and can exacerbate other deterioration mechanisms including those that occur in freeze-thaw, deicer, or sulfate exposures.

Expansive ASR begins with the formation of gel either in or on a reactive aggregate particle within the concrete. As the gel absorbs water, it can exert a fairly uniform pressure up to 10 MPa (1,450 psi) or more in all directions (Figg 1987). This pressure exceeds the tensile strength of conventional concretes, which is generally about 10% of compressive strength. The concrete cracks in a 3- or 4- pronged star pattern. This cracking is usually enough to relieve the pressure and accommodate the resulting volume increase (see Figure 3) (Figg 1987). As more particles react, cracks radiating from these “stars” join with others to form a pattern resembling a map (Poole 1992). ASR is not the only mechanism to cause map cracking; cycles of freeze-thaw or other mechanisms causing shrinking or swelling of the concrete mass can cause similar patterns. This presents a challenge to differentiating degradation due to ASR expansion from other mechanisms.

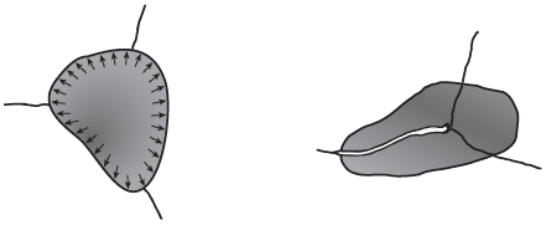

Figure 3. ASR often induces three or more cracks at each reacted aggregate particle location to relieve pressure caused by expansive force (Figg 1987).

3. ALKALI-SILICA REACTION MODELING IN GRIZZLY

Several models are developed to mathematically capture the characteristics of ASR expansion discussed in the previous section. The modeling effort can be broadly classified into one of the three following categories:

1. Micro models: Aggregate and cement paste are separately modeled and the transport equation is used to model gel formation through a two-stage process (Suwito et al. 2002). While essential to properly understand the underlying phenomena causing ASR, this level of modeling is of little relevance to the structural analysis of ASR-affected structures, because emphasis is on the transport equation for the reactants.
2. Meso models: Emphasis is on the demonstration of pessimum-sized effect (Furusawa et al. 1994).
3. Macro models: Stay clear from the transport modeling and the emphasis is on a global numerical model for the analysis of a structure. Some of the models fully decouple structural modeling from the reaction kinetics and other couple those two effects.

To model the effects of ASR on long-term performance and response of aged concrete structures, it is required to develop a fully coupled thermo-hydro-mechanical-chemical model. Among many ASR related models (developed under individual category), the thermo-chemical-mechanics model of ASR developed by Ulm et al. (2000) is widely utilized. Ulm et al. (2000) model does not include the effect of stress-state on the reaction kinetics and volumetric swelling. Farage et al. (2004) extended the Ulm et al. (2000) model by including a smeared cracking approach to model cracking of concrete from ASR expansion. However, only heat conduction was considered, the moisture diffusion was ignored in these thermo-chemical-mechanics models. In addition, these ASR models treated swelling strain to be isotropic (i.e., without stress dependency).

Saouma and Perotti (2006) presented a comprehensive couple thermo-hydro-mechanical-chemical model for ASR based on Ulm et al. (2000) model, and considered the effects of stress on the reaction kinetics and anisotropic volumetric expansion induced by ASR. Saouma and Perotti's ASR model is perhaps the most scientifically rigorous model that considers

- ASR expansion strain is treated as a full strain tensor, not calculated separately and independently for each principal direction
- ASR rate is temperature dependent
- ASR can be retarded by compressive stress within concrete structures
- Both high compressive or tensile stress state inhibits ASR expansion from the formation of micro- and macro-cracks that absorbs the expanding gel
- Triaxial compressive stress state reduces expansion
- Reduction in tensile strength and elastic modulus.

3.1 First Order Alkali-Silica Reaction Kinetics

Based on the Ulm et al. (2000) stress-independent model, Saouma and Perotti (2006) developed a first order ASR kinetics model that is dependent on both temperature and the first invariant of the stress tensor as:

$$t_C(\theta,\xi)\cdot\frac{d\xi}{dt}=\tau_C(\theta)\cdot\frac{1+\exp\left[-\tau_L(\theta,I_\sigma,f_c')/\tau_C(\theta)\right]}{\xi+\exp\left[-\tau_L(\theta,I_\sigma,f_c')/\tau_C(\theta)\right]}\cdot\frac{d\xi}{dt}=1-\xi \tag{1}$$

where $\xi(t,\theta)$ is a sigmoid curve (as shown in Figure 4) expressing the volumetric expansion in time as a function of temperature and is given by Equation (2). The value of $\xi(t,\theta)$ ranges from 0 (not reacted) to 1 (fully reacted). θ is the temperature.

$$\xi(t,\theta)=\frac{1-e^{-\frac{t}{\tau_C(\theta)}}}{1+e^{-\frac{t-\tau_L(\theta,I_\sigma,f_c')}{\tau_C(\theta)}}} \tag{2}$$

Here τ_L (Equation [3]) and τ_C (Equation [4]) are the latency and characteristic times, respectively.

$$\tau_L(\theta,I_\sigma,f_c')=f(I_\sigma,f_c')\tau_L(\theta_0)\exp\left[U_L(1/\theta-1/\theta_0)\right] \tag{3}$$

$$\tau_C(\theta)=\tau_C(\theta_0)\exp\left[U_C(1/\theta-1/\theta_0)\right] \tag{4}$$

where θ_0 is the reference temperature (i.e., the temperature at which stress-free ASR experiments are carried out); I_σ is the first invariant of the stress tensor; f_C is the uniaxial compressive strength of concrete; U_L and U_C are thermal activation energy constants to for the latency and characteristic time, respectively, and are determined from Larive's (1998) tests as

$$U_L=9400\ \pm 500K$$
$$U_C=9400\ \pm 500K \tag{5}$$

The function $f(I_\sigma,f_C)$ in Equation (3) represents the effect of compressive stress on the ASR kinetics by modifying the latency time τ_L and is defined by as

$$f(I_\sigma,f_c')=\begin{cases}1\ \ if\ I_\sigma>0\\ 1+\alpha\frac{I_\sigma}{3f_{c'}}\ if\ I_\sigma\le 0\end{cases},where\ I_\sigma=\sigma_I+\sigma_{II}+\sigma_{III} \tag{6}$$

Equation (1) for ASR is a nonlinear ordinary differential equation that can be solved locally (i.e., on the quadrature points within elements) by a Newton-Raphson iteration scheme, given the current time temperature, stress tensor, and the reaction extent at the end of the previous time step. In order to be consistent to the solid mechanics solver in the GRIZZLY code, the incremental strain (stress) formulation approach was adopted. Equation (1) is reformulated in terms of incremental ASR extent $\Delta\xi$ from time t to $t+\Delta t$ and written in residual form as:

$$F(\xi)=t_C\left(\theta^{t+\Delta t},\xi^{t+\Delta t}\right)\cdot\frac{\xi^{t+\Delta t}-\xi^t}{\Delta t}-1+\xi^{t+\Delta t}$$
$$=t_C\left(\theta^{t+\Delta t},\xi^t+\Delta\xi^{t+\Delta t}\right)\cdot\frac{\Delta\xi^{t+\Delta t}}{\Delta t}-1+(\xi^t+\Delta\xi^{t+\Delta t}) \tag{7}$$

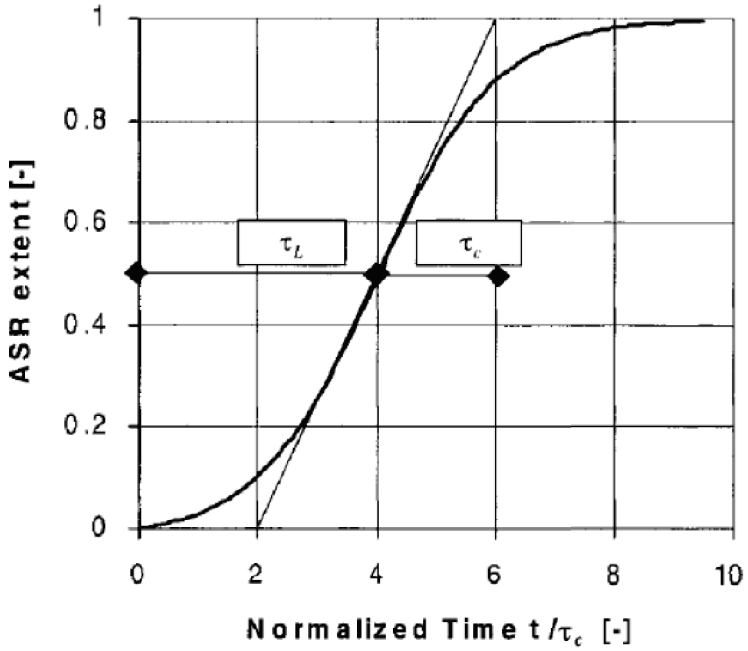

Figure 4. Definition of latency and characteristic time in normalized isothermal expansion curve (Ulm et al. 2000).

3.2 Stress-Dependent Alkali-Silica Reaction Volumetric Strain

Once the increment of ASR extent $\Delta\xi$ is obtained, the ASR volumetric strain increment $\Delta\varepsilon_{vol}^{ASR}$ is then evaluated by the following formula

$$\Delta\varepsilon_{vol}^{ASR} = \Gamma_t(f_t', \sigma_I|COD)\Gamma_C(\bar{\sigma}, f_c')g(H)\Delta\xi\varepsilon^{\infty}|_{\theta=\theta_0} \tag{8}$$

where f_t' is the tensile strength of the concrete; σ_I is the maximum principal stress (> 0 under tensile stress); COD is the crack opening displacement; σ is the ratio between the hydrostatic stress and compressive strength of concrete, and ε^{∞} is the laboratory-determined maximum free volumetric expansion at the reference temperature θ_0. The function $g(H)$ in Equation (6) accounts for the dependency of gel expansion from the presence of water in concrete and take the form of (as defined in Saouma (2014))

$$g(H) = H^m \tag{9}$$

where the exponent m is an empirical constant and H is the relative humidity in concrete. $g(H)$ has a value between 0 and 1. For concrete dam studies, one can reasonably assume $g(H)$ has a value of 1.

However, for various concrete structures, $g(H)$ has to be determined by either laboratory experiments or parameter fittings. Function $\Gamma_t(f_t', \sigma_I|COD)$ in Equation (10) accounts for the reduction of ASR expansion due to tensile cracking (e.g., gels are adsorbed into tensile macrocracks) and takes the following form:

$$\Gamma_t = \begin{cases} Elasticity & \begin{matrix} 1 \\ \Gamma_t + (1-\Gamma_r)\frac{\gamma_t f_t'}{\sigma_I} \end{matrix} & \begin{matrix} if\ (\sigma_I \le \gamma_t f_t') \\ if\ (\gamma_t f_t' \le \sigma_I) \end{matrix} \\ Smeared\ crack & \begin{matrix} 1 \\ \Gamma_t + (1-\Gamma_r)\frac{\gamma_t W_C}{COD_{max}} \end{matrix} & \begin{matrix} if\ (COD_{max} \le \gamma_t f_t' < \sigma_I) \\ if\ (Y_t W_C < COD_{max}) \end{matrix} \end{cases} \tag{10}$$

Here γ_t is the fraction of the tensile strength beyond which gel is absorbed by cracks and is a user input parameter in simulation and Γ_r is a residual ASR expansion retention factor for ASR under tension. In the current GRIZZLY code, ASR swelling model was implemented in conjunction with the elasticity solid mechanics model. Although in GRIZZLY code, a smeared crack model was already implemented for solid mechanics, but the function Γ_t was implemented under elasticity mode. Function $\Gamma_C(\bar{\sigma}, f_c')$ in Equation (11) accounts for the reduction in ASR volumetric expansion under compressive stress state, where the gel is absorbed by diffused microcracks and takes the following form:

$$\Gamma_C = \begin{cases} 1 & if\ \bar{\sigma} \le 0 \quad tension \\ 1 - \frac{e^{\beta}\bar{\sigma}}{1+(e^{\beta}-1)\bar{\sigma}} & if\ \bar{\sigma} > 0 \quad compression \end{cases}$$

$$\bar{\sigma} = \frac{\sigma_I+\sigma_{II}+\sigma_{III}}{3f_c'} \tag{11}$$

Here the exponent β is an empirical constant (between -2 and 2 according to Saouma (2014)) and σ is the ratio between the hydrostatic stress and compressive strength of concrete.

3.3 Anisotropic Alkali-Silica Reaction Strains and Weights in Principal Directions

The incremental ASR volumetric strain $\Delta\varepsilon^{ASR}$ needs to be redistributed along three principal directions according to their relative propensity to expansion. Saouma and Perottie (2006) presented a method to calculate the relative weights along three principal directions based on the principal stresses under uniaxial, biaxial, or triaxial confinement conditions. This subsection provides details of their approach for calculating the redistribution weights of ASR volumetric strain in principal directions and its implementation in GRIZZLY code. Here again, the notations of Saouma and Perottie (2006) were followed.

Given the full stress tensor (in Cartesian coordinates) on a quadrature point within an element, an Eigen solver is used to obtain the three principal stresses σ_k, σ_l, and σ_m, and associated Eigen-vectors for the directions of principal stresses R_k, R_l, and R_m. These Eigen-vectors form a stress/strain rotational matrix $R = R(R_k, R_l, R_m)$ that will be used later to rotate the incremental ASR strain tensor expressed in principal stress/strain coordinates back into Cartesian coordinates.

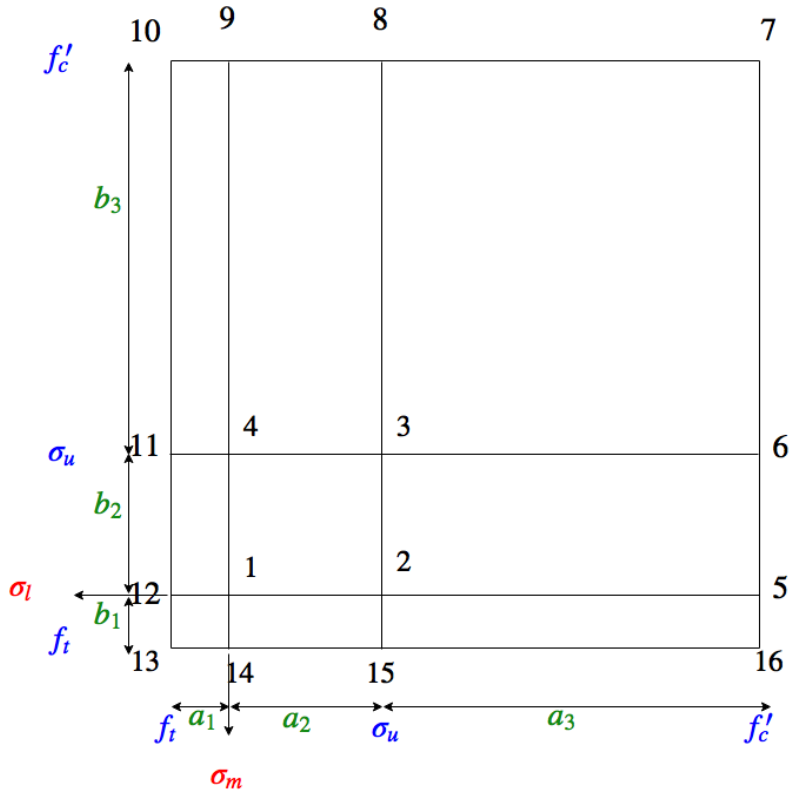

Figure 5. Weight regions (Saouma and Perottie 2006).

The weight allocation scheme for the principal directions starts with dividing the stress space into nine quadrants using concrete tensile strength f_t, compressive strength f_c, and a gel expansion inhibiting compressive stress σ_u (shown in Figure 5). σ_u is defined as the compressive stress beyond which no further gel expansion can occur. Saouma and Perottie (2006) proposed a value of -10MPa based on previous experimental studies. Any combinations of two principal stresses will fall into one of nine quadrants on this two-dimensional stress map. There are a total of 16 nodes.

In order to calculate the ASR expansion weight along the direction of a particular principal stress, σ_k for example, the following steps are needed:

- Identify the quadrant encompassing the other two principal stresses σ_l and σ_m using Figure 5 and the corresponding nodal numbers of that quadrant
- Go to the Table 1 rows corresponding to the identified nodal numbers, then determine the nodal weights $W_i(\sigma_k)$, $i = 1, 2, 3, 4$ from the last 3 columns of Table 1 in the corresponding rows by a linear interpolation of σ_k.

Table 1. Triaxial weights (Saouma and Perottie (2006)).

			Weight direction k		
Nodal number	σ_l	σ_m	$\sigma_k \leq 0$	$\sigma_k = \sigma_u$	$\sigma_k = f'_c$
1	0	0	1/3	0	0
2	σ_u	0	1/2	0	0
3	σ_u	σ_u	1	1/3	0
4	0	σ_u	1/2	0	0
5	f_c	0	1/2	0	0
6	f_c	σ_u	1	1/2	0
7	f_c	f_c	1	1	1/3
8	σ_u	f_c	1	1/2	0
9	0	f_c	1/2	0	0
10	f_t	f_c	1/2	0	0
11	f_t	σ_u	1/2	0	0
12	f_t	0	1/3	0	0
13	f_t	f_t	1/3	0	0
14	0	f_t	1/3	0	0
15	σ_u	f_t	1/2	0	0
16	f_c	f_t	1/2	0	0

Finally, compute the ASR expansion weight $W_k(\sigma_k, \sigma_l, \sigma_m)$ for the principal direction k using the four nodal weights of the quadrant where (σ_l, σ_m) falls by a bilinear interpolation:

$$W_k(\sigma_k, \sigma_l, \sigma_m) = \sum_{i=1}^{4} N_i(\sigma_i, \sigma_m) W_i(\sigma_k) \tag{12}$$

where N_i is the bilinear shape function similar to those used in finite element method and is given by

$$N(\sigma_l, \sigma_m) = \frac{1}{ab}[(a-\sigma_l)(b-\sigma_m), \sigma_l(b-\sigma_m), \sigma_l\sigma_m, (a-\sigma_l)\sigma_m]$$

$$W(\sigma_k) = [W_1(\sigma_k), W_2(\sigma_k), W_3(\sigma_k), W_4(\sigma_k)]^T$$

$$a = (a_1|a_2|a_3)\ b = (b_1|b_2|b_3)$$

$$\sigma_l = (\sigma_l|\sigma_l - \sigma_u)\ \sigma_m = (\sigma_m|\sigma_m - \sigma_u) \tag{13}$$

The previous steps are then repeated for the ASR expansion weights along other two principal directions, $W_l(\sigma_k, \sigma_l, \sigma_m)$ and $W_m(\sigma_k, \sigma_l, \sigma_m)$. Note that the summation of W_k, W_l, and W_m equals 1. The individual incremental ASR strains along the principal directions are then obtained using these relative weights by the following formula:

$$\Delta\varepsilon_i^{ASR} = W_i \Delta\varepsilon_V^{ASR}, i = 1, 2, and\ 3 \tag{14}$$

Unlike those isotropic ASR swelling models, the incremental ASR strains along principal directions obtained by the above formula are in general different from each other, depending on the local stress state and material confinement conditions.

Finally, the full ASR expansion-induced incremental strain tensor $\Delta\varepsilon^{ASR}$ on quadrature points can then be conveniently obtained by rotating $\Delta\varepsilon^{ASR}$ into the current coordinates via

$$\Delta\varepsilon^{ASR} = R\{\Delta\varepsilon_i^{ASR}\}R^T \tag{15}$$

$\Delta\varepsilon^{ASR}$ is a chemically-imposed incremental strain on each quadrature point, which is used by the solid mechanics model in GRIZZLY to drive the deformation of concrete structures.

3.4 Reduction of Elastic Modulus and Tensile Strength

The ASR-induced deterioration of concrete mechanical properties is simply modeled as time-dependent function of ASR extent ξ(t, θ) following Saouma and Perottie (2006).

$$\begin{aligned} E(t,\theta) &= E_0[1-(1-\beta_E)\xi(t,\theta)] \\ f_t(t,\theta) &= f_{t,0}[1-(1-\beta_f)\xi(t,\theta)] \end{aligned} \tag{16}$$

where E_0 and $f_{t,0}$ are the original elastic modulus and tensile strength, respectively; and $\beta_E$and β_f are the corresponding residual fractional values when the concrete has fully reacted (i.e., ε_{ASR} tends to $\varepsilon_{ASR}^{\infty}$). Both β_E and β_f are input parameters by user.

In a quick summary, during each timed step, within each globe nonlinear/linear iteration, on each quadrature point within each element, an incremental ASR extent Δξ is calculated first using current temperature and relative humidity by numerically solving Equation (1); then an incremental ASR volumetric expansion and incremental ASR volumetric strain $\Delta\varepsilon_{vol}^{ASR}$ are computed next using Equation (8), followed by the calculation of expansion redistribution weights for principal directions using Equation (12); and finally the full ASR-induced incremental strain tensor is obtained using Equation (15).

3.5 Validation

Multon (2003) presented experimental measurements of concrete samples subjected to ASR swelling under various stress states to better quantify the effect of stress on ASR expansion anisotropy. These experimental measurements are used to validate the anisotropic ASR swelling model implemented in GRIZZLY. In the Multon (2003) experiments, stacks of steel rings confine cylindrical samples of 130 mm in diameter and 240 mm in height (shown in Figure 6). In the experiments, two types of steel rings (3 mm and 5 mm thick) were used. In this section, the data obtained from the tests using 3-mm-thick steel ring confinements is arbitrarily selected to compare against the simulations. Also, it is worth noting the stacks of steel rings are used to provide lateral confinements; thus, the steel rings do not provide any constraint to the movement of samples along the axial direction. A frictionless contact model between the samples and steel rings is adopted during our simulations. Two levels of the applied axial loading stresses, 0 and 10 MPa, are chosen from experiments to compare against simulations.

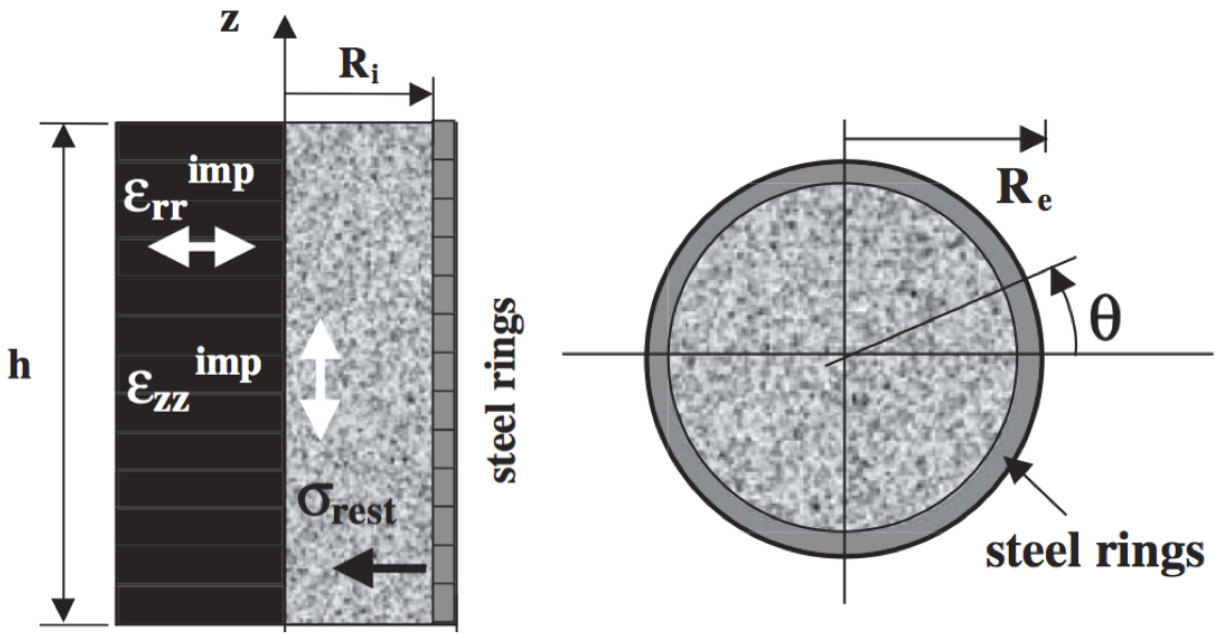

Figure 6. Schematic description of Multon's ASR expansion experiments (Multon, 2003): (left) axial view and (right) plane view.

Similarly, due to the symmetries of the sample geometry and loadings, the problem was modeled using a two-dimensional axial symmetric model with half of the height of the samples, a roller boundary on the bottom (zero displacement in axial direction), and a roller boundary on the left (zero displacement in radial direction). All tests were carried out under isothermal conditions (room temperature) and assumed constant and uniform relative humidity for all samples. Thus, the problem is decoupled from the thermal and moisture diffusion processes. All the mechanical deformations of samples are induced by the axial loadings (if any) and ASRs.

In this subsection, simulation results and comparisons with Multon (2003) ASR expansion tests with steel ring confinement are provided. Figure 3 shows the geometry and boundary conditions of the two-dimensional axial-symmetric model and the mesh used in the simulation. The yield stress of 206 MPA is observed on a steel ring when assigned with Young's modulus of 193 GPa and Poisson's ratio of 0.3. Since the steel rings were not connected during the experiments, there is no constraint of rings on the axial movement of the samples. To more realistically represent this experimental setup, a frictionless contact model implemented in the solid mechanics model of GRIZZLY code is used for better represent the constraint from steel rings.

The case of 10 MPa axial load is used here as an example to illustrate the displacement, ASR strain, and stress fields. The samples are under true triaxial stress state when the axial load was applied during the experiment. Two important parameters, α and β, representing the retardation of reaction kinetics and the reduction of ASR-induced expansion when the samples are under compressive stress state, need to be adjusted to match the experimental data. The measured lateral strains of the samples subjected to 10 MPa axial load were used to calibrate the ASR model. The final optimal values for α and β are 4.3 and 1.5, respectively, which yields the best match with the experimental data. Figure 7 shows the simulated axial and lateral stress fields at time of 400 days. Notice the axial stress in the cement is 10 MPa as expected to be equal to the applied load, and uniform everywhere. The lateral (or radial) stress is about -4.7 MPa, smaller that the axial stress and uniform everywhere within the samples. The axial stress for steel rings is 0, which is consistent with the frictionless contact model we used for concrete-steel interface.

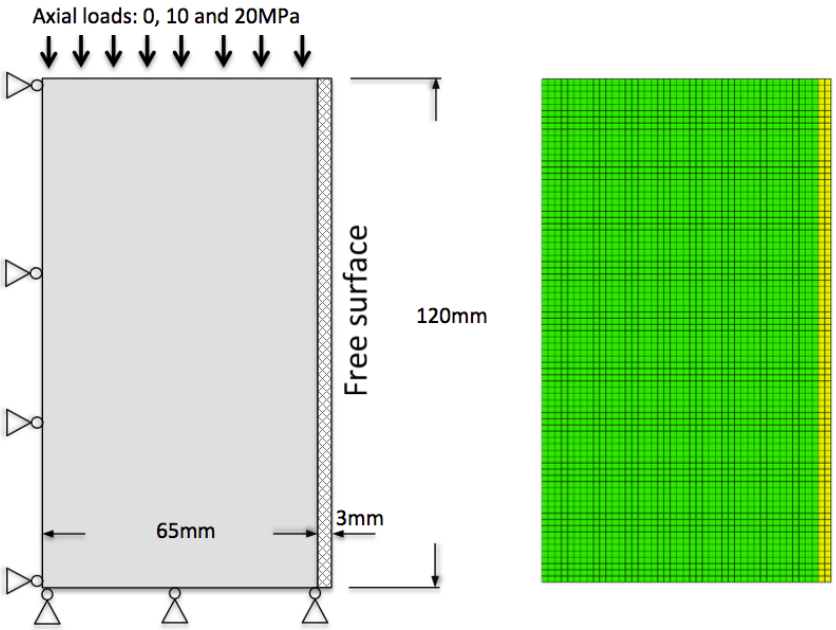

Figure 7. Geometric and boundary conditions (left) and finite element mesh (right) for simulating the ASR expansion experiments with steel ring confinement.

3.6 Results

Figure 8 shows the simulated axial and lateral stress fields at 400 days. Notice the axial stress in the cement is 10 MPa as expected to be equal to the applied load and uniformly elsewhere. The lateral (or radial) stress is about -4.7 MPa smaller than the axial stress and uniform everywhere within the samples. The axial stress for steel rings is 0, which is consistent with the frictionless contact model used for concrete-steel interface.

Figure 9 shows the simulated axial and lateral displacement fields at time of 400 days. Notice that the discontinuity of the axial displacement field across the concrete-steel ring interface is due to the frictionless contact model used in the simulations. However, the simulated lateral displacement is continuous across the concrete-steel interface.

Figure 10 shows the simulated axial and lateral ASR strains (e.g., the chemical strains imposed onto the concrete structures) at 400 days. Notice that the axial ASR strain is about 1 order of magnitude smaller than the lateral ASR strain from much higher stress in the axial direction than the lateral direction. ASR was only considered in the concrete samples. There is no ASR-induced strain in the simulation results for steel rings.

Figure 11 shows the detailed comparison of simulated and measured lateral strains for the samples confined by 3 mm-thick steel rings and subjected to 10 and 20 MPa axial loads. For the case of the 10 MPa axial load, the simulated lateral strain agrees with the experiment very well. This is not surprising since the model was calibrated to the data measured at 10 MPa axial load. When using the same parameter values of α and β to simulate the experiments with 20 MPa axial load, reasonably satisfactory can be matched to the experimental data.

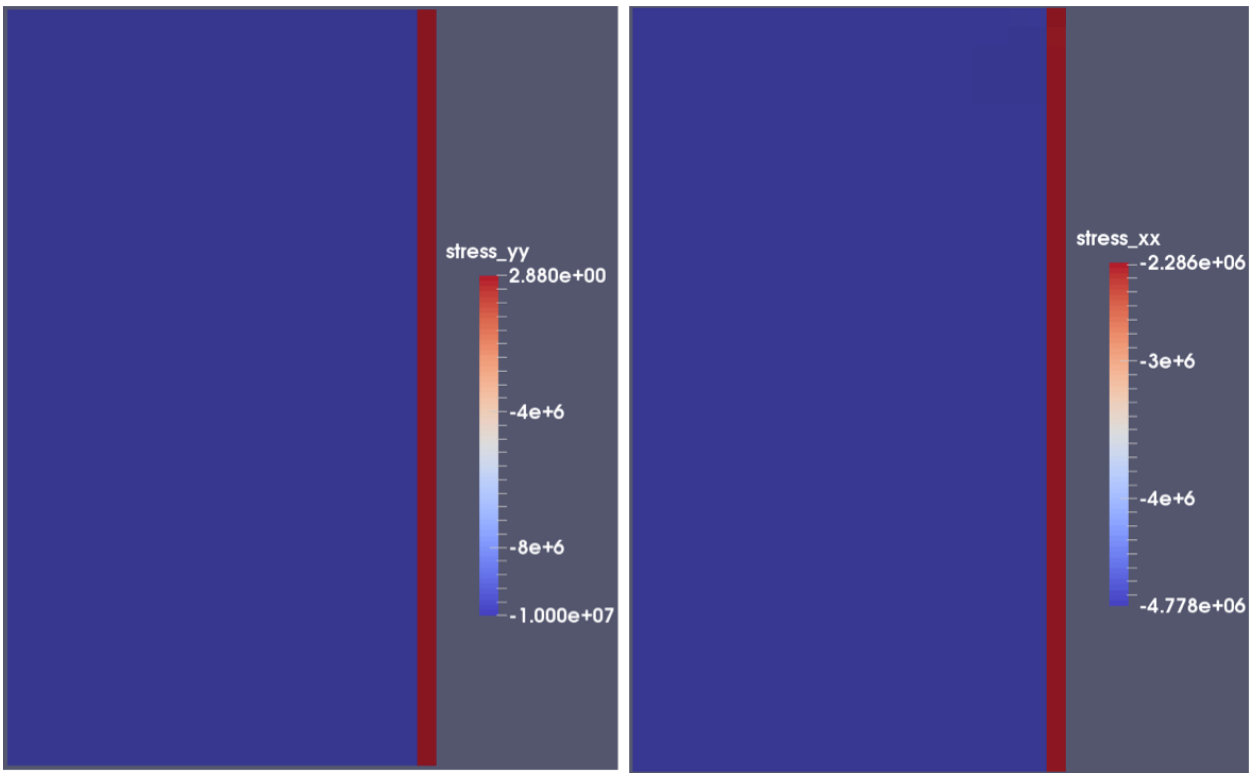

Figure 8. The axial (left) and lateral (right) stresses at 400 days.

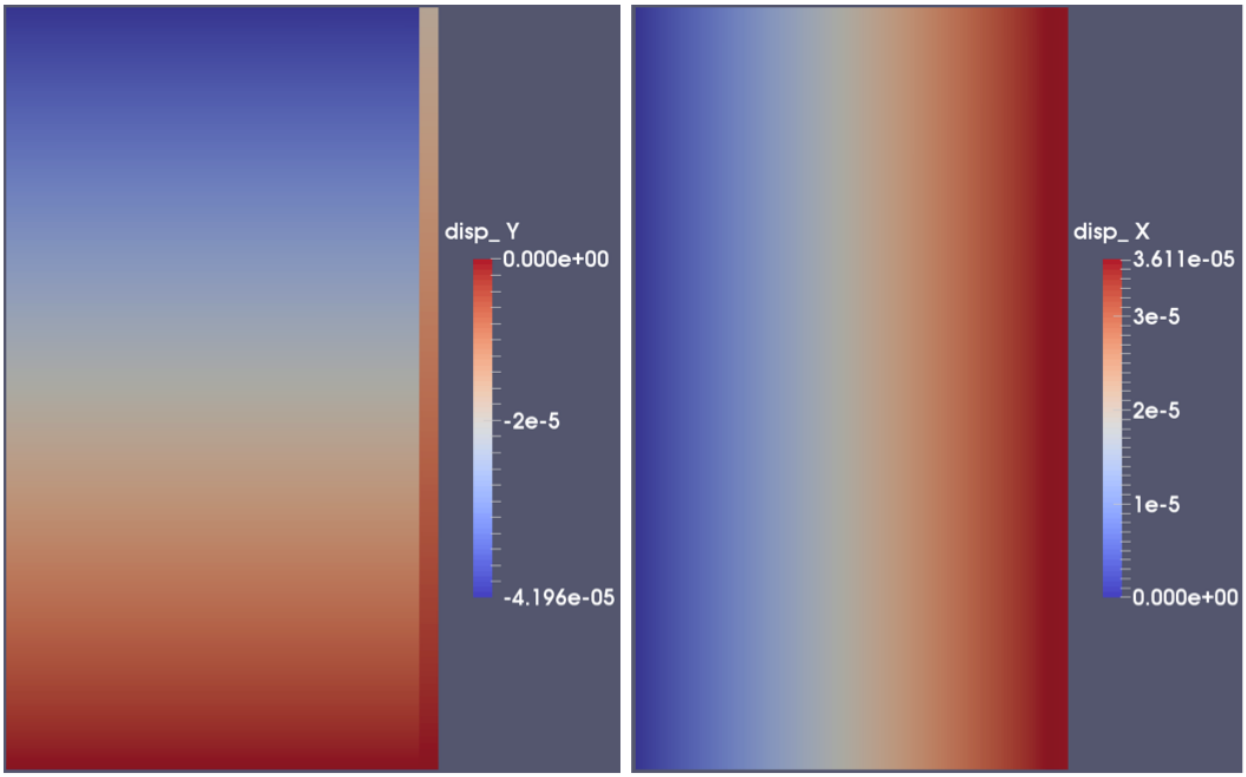

Figure 9. The axial (left) and lateral (right) displacements at 400 days.

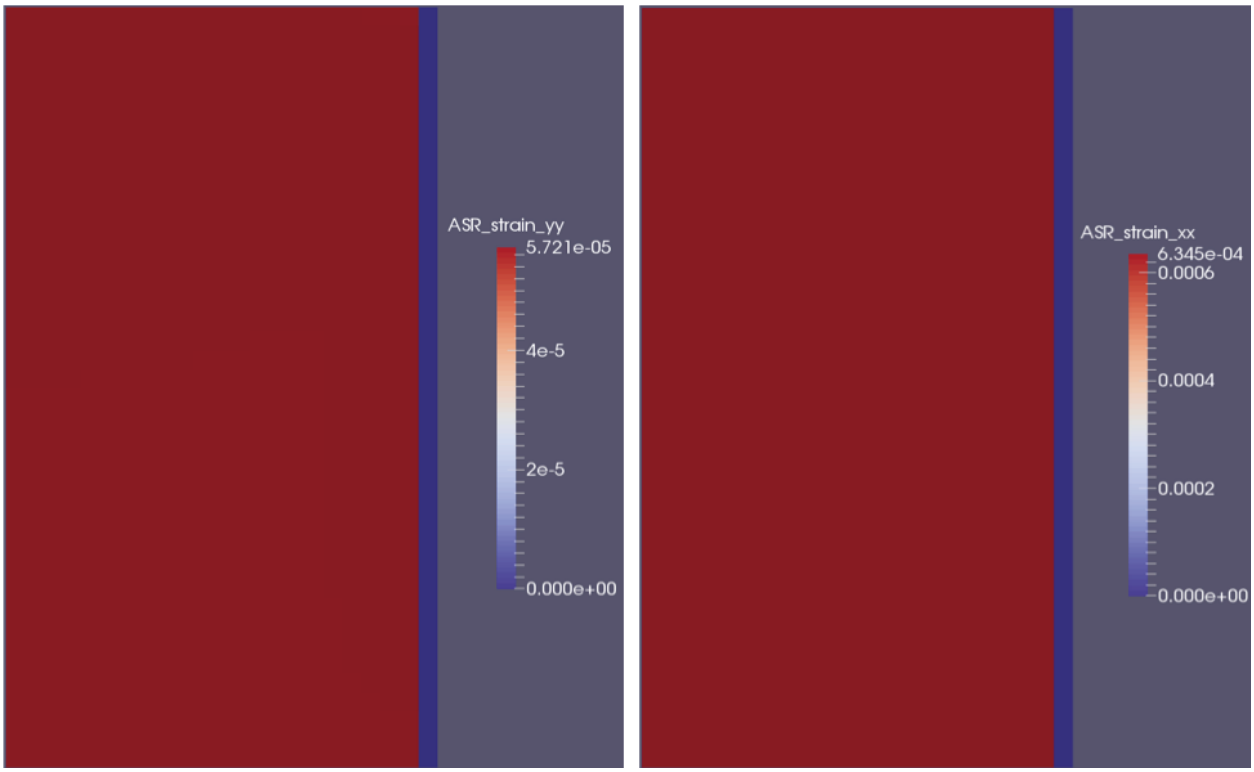

Figure 10. The axial (left) and lateral (right) ASR strains at 400 days.

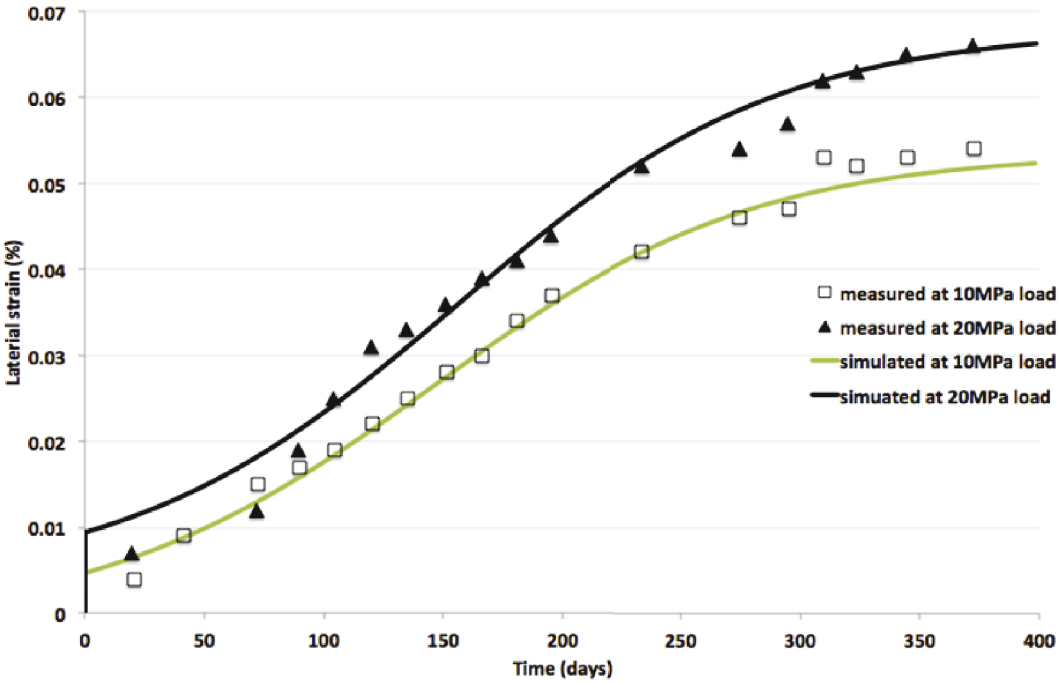

Figure 11. Comparisons between the simulated and measured lateral strains for confined samples at 10 and 20 MPa axial loads.

4. PERCOLATION MODELING OF ALKALI-SILICA REACTION

The percolation models have an intuitive appeal from their simple yet powerful modeling capabilities. The simplest two-dimensional percolation model is shown in Figure 12. It is 11 × 11 lattice where each site can be in one of two states, occupied or empty.

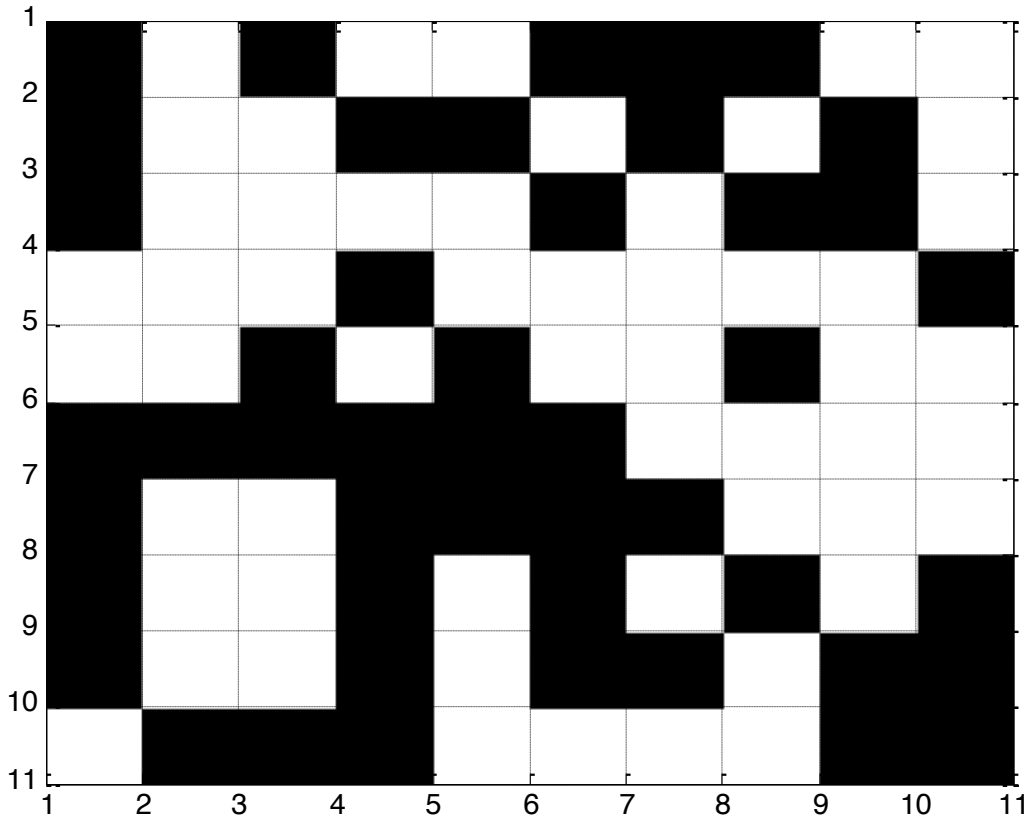

Figure 12. Example of site percolation on a square lattice.

Each site is occupied independently of its neighbors with probability p. This percolation model is called site percolation. The occupied sites are either isolated or form groups. A group of occupied sites is called a cluster. The study of two-dimensional site percolation revolves around existence of a percolating or a spanning cluster, which extends from one side of the lattice to another. For small p, similar to the one depicted in Figure 12 where $p = 0.3$. There is no spanning cluster, while for p close to 1, the existence of the spanning cluster is guaranteed. The p value at which the spinning cluster first appears is called critical probability and it plays a fundamental role in the theory of geometrical phase transitions. In the limit of an infinite lattice, there exists a well-defined threshold probability p_c such that:

for $p < p_c$, no spanning cluster exists

for $p \geq p_c$, a spanning cluster exists.

At $p = p_c$ the system is in a critical state when there are long range correlations that cause a sudden switch from non-percolating to percolating state. At this critical point, it is impossible to distinguish between percolating and non-percolating states and phase boundaries cease to exist. This transition is a phase transition and for material science it is a transition from a healthy structure to a faulty structure.

While the existence of a percolating cluster at $p = p_c$ can be demonstrated; theoretically, it is practical discovery on a finite lattice is not a trivial task and a number of cluster labeling algorithms have been proposed to tackle the problem. At critical probability, the system demonstrates scaling behavior (i.e., it looks the same at different scales). This property is called a fractal property of the percolating lattice. In fact, the number of clusters *n* having the exact size of *s* occupied cells follows a power law $n = s^{-\tau}$, where τ is the critical exponent. This means that the ratio of the number of clusters of two different sizes is independent of the cluster size. Thus, percolating clusters are self-similar or free of scale. Due to the self-similarity, the analysis of percolation lattice is rather complicated and usually involves a renormalization approach.

Many natural phenomena show evidence of some degree of power law behavior. However, the provenance of this behavior remains a mystery. One of the most persistent correlation patterns observed in a wide variety of systems encompassing different scientific disciplines is the ubiquitous $1/f^{\propto}$ noise, which is characterized by the power of the signal at given frequencies to be inversely proportional to the frequencies. Notice that the percolation cluster distribution $n = s^{-\tau}$ follows exactly this law with cluster size playing the role of frequency. The existence of $1/f^{\propto}$ noise has been reported in numerous fields ranging from medicine to engineering.

Among engineering processes where $1/f^{\propto}$ noise has been observed is crack development and propagation in structures. The pervasiveness of $1/f^{\propto}$ -like behavior is intriguing and raises the possibility of existence of some general (albeit unknown) mechanism responsible for generation of this type of dependencies.

Since the discovery of the general nature of $1/f^{\propto}$ noise, numerous attempts have been made to elucidate its etiology and origins. The most trivial and readily available explanation for the existence of $1/f^{\propto}$ in engineering is the low-pass filtering nature of many engineering structures, when the signal of interest is repeatedly convolved with impulse response functions representing different compartments. However, such an explanation lacks universality as many directly observable engineering variables display $1/f^{\propto}$ pattern. Another possible mechanism to explain the ubiquitous nature of $1/f^{\propto}$ noise is intermittency, which is the alternation of chaotic and regular dynamics exhibited by the solution of certain differential equations. Although intermittency generates $1/f^{\propto}$ spectra, it has been observed only in simulations. One more mechanism proposed to explain the occurrence of $1/f^{\propto}$ in engineering is multiscaled randomness, which represents physiological signals as the summation of different random inputs, generated by different regulatory mechanisms. This model has been shown to produce $1/f^{\propto}$ spectra with various scaling components; however, under tight constraints imposed on the model's parameters. Because engineering parameters can vary widely, this model cannot be considered as the only mechanism responsible for $1/f^{\propto}$ behavior in engineering systems. The most audacious and bold attempt to explain the omnipresent occurrence of $1/f^{\propto}$ noise had been undertaken by P. Bak and his colleagues several years ago. Departing from the observation that in many cases $1/f^{\propto}$ noise occurs in physical systems, which are in critical or unstable conditions, they suggested the concept of self-organized criticality. In contrast to the criticality observed in physical systems, where a parameter needs to be tuned to drive the system in a critical state, Bak et al. (1987, 1997) suggested that many natural and man-made systems drive themselves into critical states without any exogenous tuning of the parameters. Although this model generated a lot of response among scientific community, it has been discovered later that the self-organized criticality cannot be considered to be a ubiquitous mechanism because it can generate other types of signals, different from the $1/f^{\propto}$ noise. In addition, it proved that the self-organized criticality can be reliably observed in computer simulation, but its occurrence in real physical system was less convincing (Turcotte, Smalley, and Solla 1985).

Our current research concerns occurrence of $1/f^{\alpha}$ noise in concrete structures and also interrelations of this type of noise across different types of material. In this report, percolation $1/f^{\propto}$-like behavior is proposed to explain and model of the initiation and growth of the ASR in concrete. The occurrence of

$1/f^{\propto}$ spectra in these reactions would imply that there are strong long-range correlations among ASR contaminated sites. The analysis of the system with strong long-range correlations can be performed using the renormalization group approach.

The renormalization group approach (Smalley, Turcotte, and Solla 1985) involves merging neighboring occupied cells into a bigger cell depending on how many cells are occupied within the initial cluster. This process will converge to either an empty lattice or to a completely occupied lattice depending on initial configuration. Depending on the final state, a conclusion about the existence of the percolating cluster can be made. Most importantly, the correlation length of the lattice configuration can be deduced and then a decision about its criticality can be made.

4.1 Application of Percolation Theory to Concrete

Site percolation theory is applied here. In the finite element structure, each cell is marked as occupied or not occupied. Then, the Hoshen-Kopelman algorithm is used to examine whether the structure is under phase transient or not. The Hoshen-Kopelman algorithm procedure is listed below:

- For each cell, mark with 0 or 1 (occupied) based on criteria (e.g., mark as 1 if a cell value [calculated randomly sampled] is greater than threshold p).
- In a specific order (e.g., two-dimensional, from bottom to top, from left to right), for an occupied cell.
- If it has no occupied neighbors, assign a new label that has not yet been used.
- If it has one occupied neighbor, assign to the current cell the same label as the occupied neighbor.
- If it has more than one occupied neighbor, assign the current cell using the lowest numbered cluster label (min_label), and reassign the cluster, which contains a higher-numbered neighbor with min_label. As shown in Figure 13, the first two cells at coordinates (0, 3) and (1, 3) are labeled by 2, then they are reassigned by the min_label (1) when the cell at location (2, 3) is connecting its neighbors.

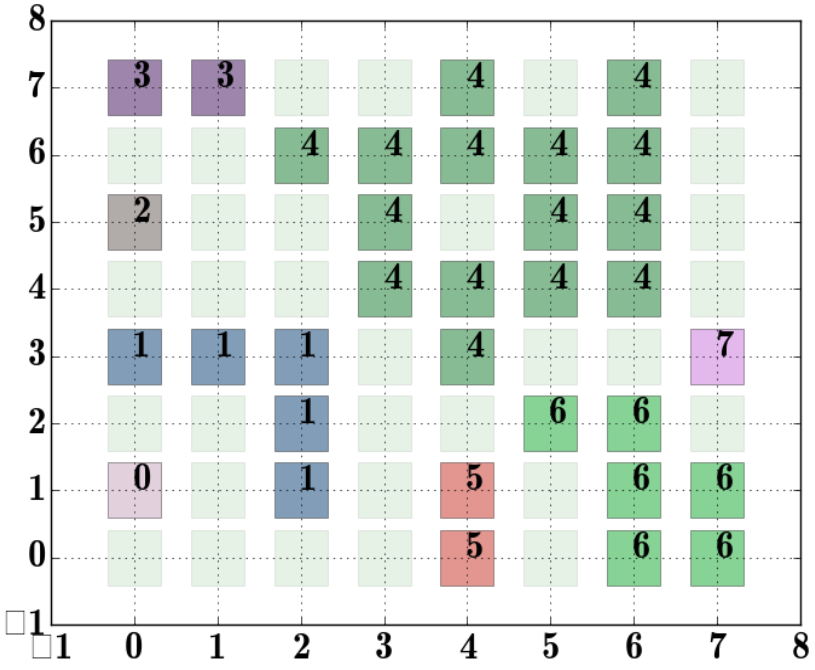

Figure 13. Hoshen-Kopelman algorithm for percolation theory.

Figure 14 shows the two-dimensional percolation model. The three-dimensional case can be realized in a similar procedure.

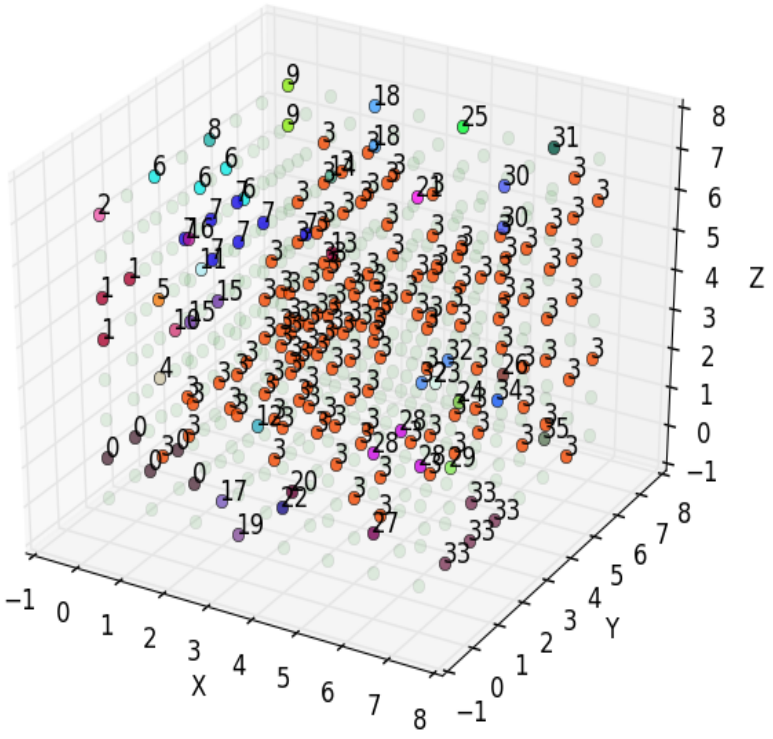

Figure 14. Three-dimensional percolation theory.

The indication of phase transient is discussed above. In the percolation theory, the threshold p is needed as a material parameter. By applying BN calibration, p can be calibrated via compare the relations between maximum cluster size and percolation threshold.

4.2 Random Field as Boundary Conditions

In realistic, boundary conditions in concrete modeling are not uniformly distributed. In other words, it is random. In two- or three-dimensional cases, the boundary condition can be treated as a random field. Random fields can be generated in different ways. Here, the Gaussian Markov Random Field is generated for this purpose. The algorithm is listed below:

a. Construct the mean vector $\mu = (\mu_1, \mu_2, \ldots, \mu_n)^T$ and covariance matrix $\Sigma = (\Sigma_{ij})$ by setting $\mu_i = \hat{\mu}_{t_i}, i = 1, \ldots, n$ and $\Sigma_{ij} = \hat{\Sigma}_{t_i,t_j,i,j=1,\ldots,n}$.

b. Find a square root A of Σ, so that $\Sigma = AA^T$.

c. Generate $Z_1, \ldots, Z_n \sim N(0,1)$. Let $Z = (Z_1, \ldots, Z_n)^T$.

d. Output $\boldsymbol{X} = \mu + A\boldsymbol{Z}$

The exponential covariance function used in the algorithm is computed using Equation (17)

$$Cov(\widehat{X_s}, \widehat{X_t}) = exp\{-c||s-t||_T^{\alpha}\} \quad (17)$$

Both temperature and humidity boundary conditions can be simulated using Gaussian Markov Random Field (Figures 15 and 16). A two-dimensional concrete ASR model is created to show how percolation works. As shown in Figure 17, a two-dimensional concrete plate is modeled in GRIZZLY. All the material parameters are used in the demonstration simulation is taken from the built-in GRIZZLY library. For this two-dimensional structure, 8 × 8 cell mesh is generated.

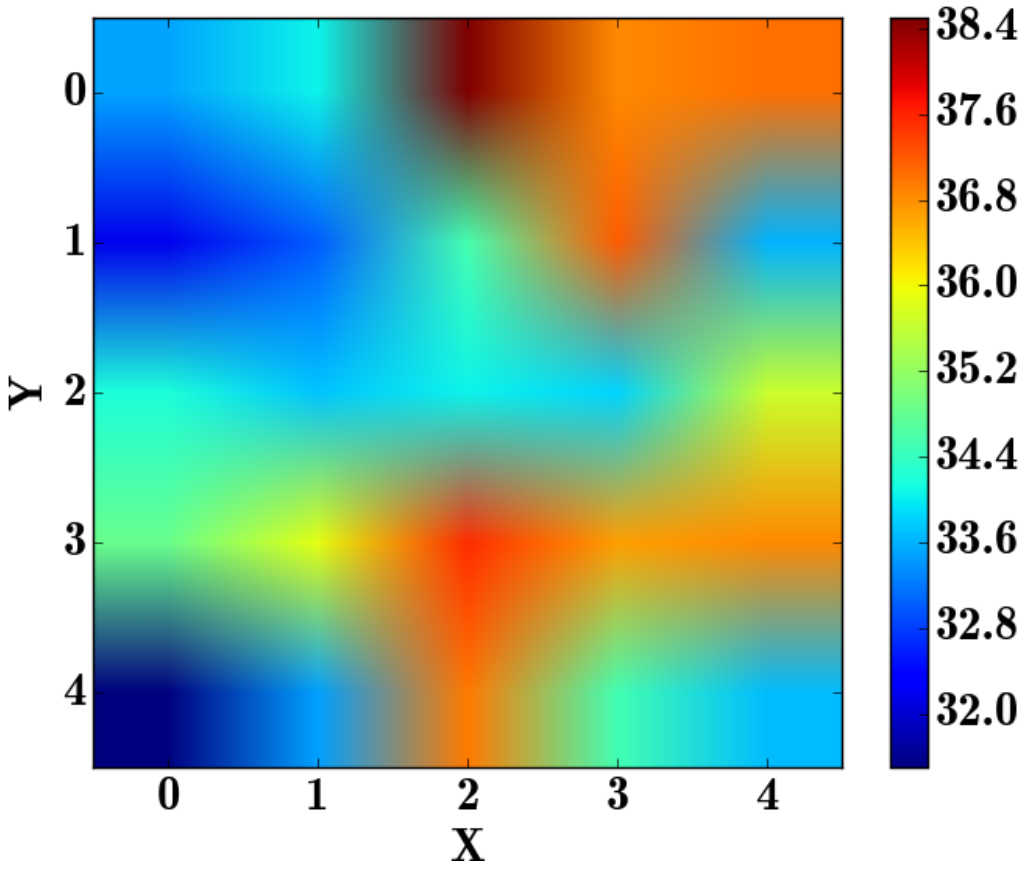

Figure 15. Random field for temperature.

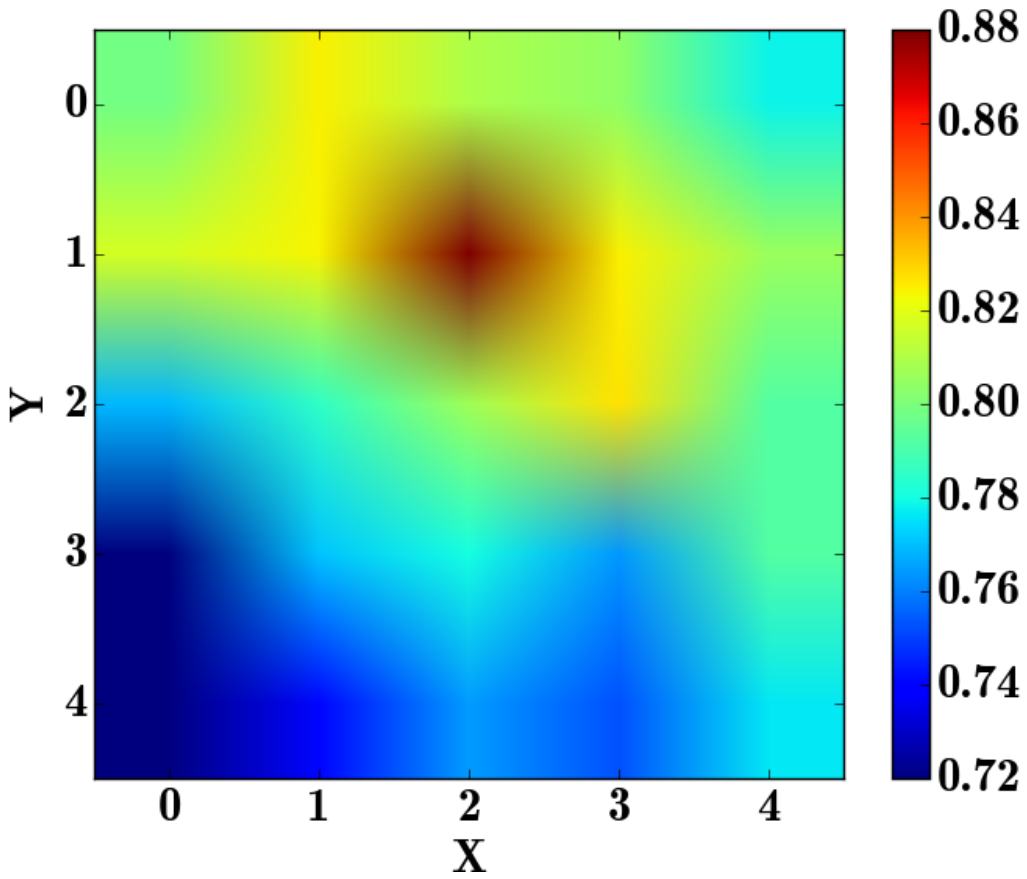

Figure 16. Random field for relative humidity.

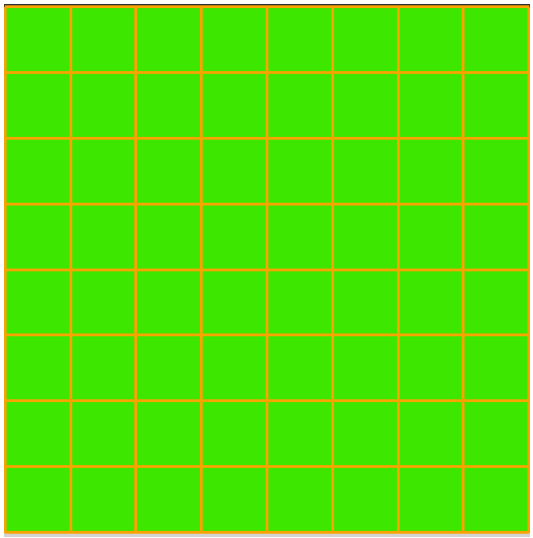

Figure 17. Mesh for two-dimensional demonstration problem.

After implemented in GRIZZLY, the ASR extent for each cell can be extracted by using the Hoshen-Kopelman algorithm (Figure 18) and also maximum cluster size for different values of percolation threshold (see Figure 19).

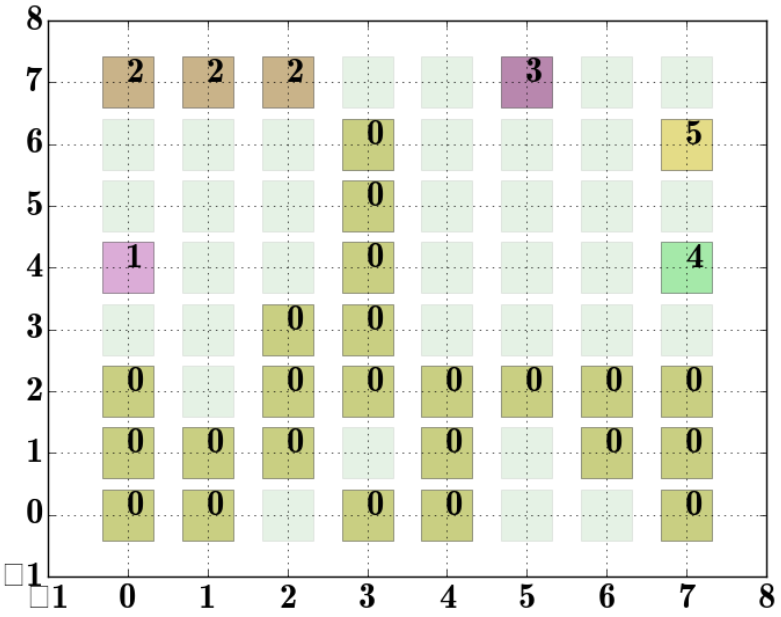

Figure 18. Phase transition pattern.

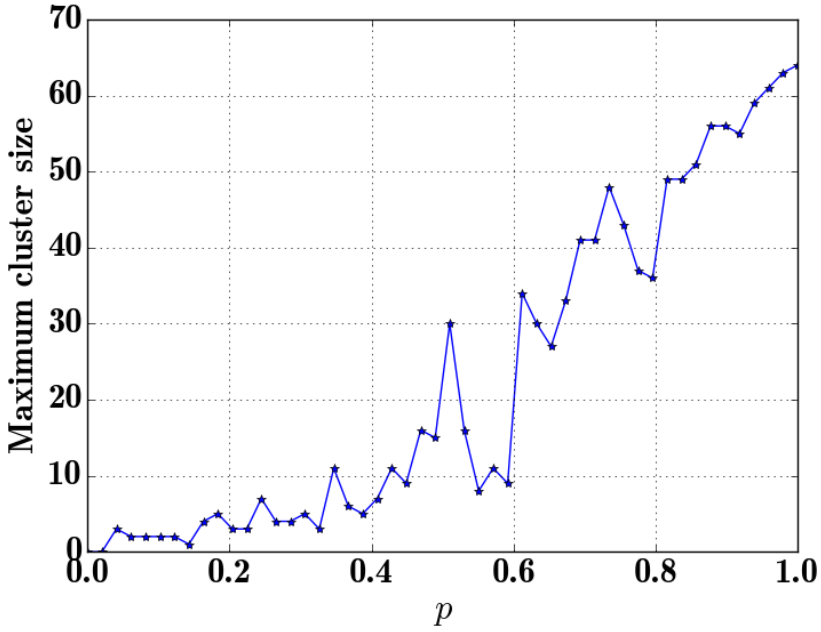

Figure 19. Maximum cluster size versus percolation threshold.

5. CONCRETE SAMPLES WITH EMBEDDED GLASS

A laboratory experiment is conducted to investigate the effectiveness of infrared thermal imaging in detecting ASR gel formation in a cement slab. Glass is basically silica with a strong ability to form ASR and provides a quick proof-of-concept for the proposed prognostics and health management framework. The silica in glass reacts with the calcium in cement to form calcium silicate hydride (which is ASR gel) in the presence of NaOH. In the case of aggregate, the reactivity depends on several factors such as mineralogy, aggregate size, etc.; thus, the time taken to form ASR gel is variable. Another important point is the regular geometric shape of the glass slides and the simplified ability to control their embedding location in the sample.

5.1 Casting of the Concrete Samples with Embedded Glass

Two sets of three samples each sized 9 in. × 5 in. × 2 in. were cast. Water-cement ratio of 0.4 was used for these samples to achieve adequate workability in cement paste. ASR is a chemical reaction between siliceous constituents found in concrete aggregates and hydroxyl ions within the concrete. For better control with test samples, aggregates were replaced by glass (approximately 75% silicon dioxide, SiO_2) in these experiments. Each set has three types of samples:

(i) Sample with only cement (A1, A2)
(ii) Sample with cement and one glass plate near the top (B1, B2)
(iii) Sample with cement and three glass slides of various thicknesses in the middle (C1, C2).

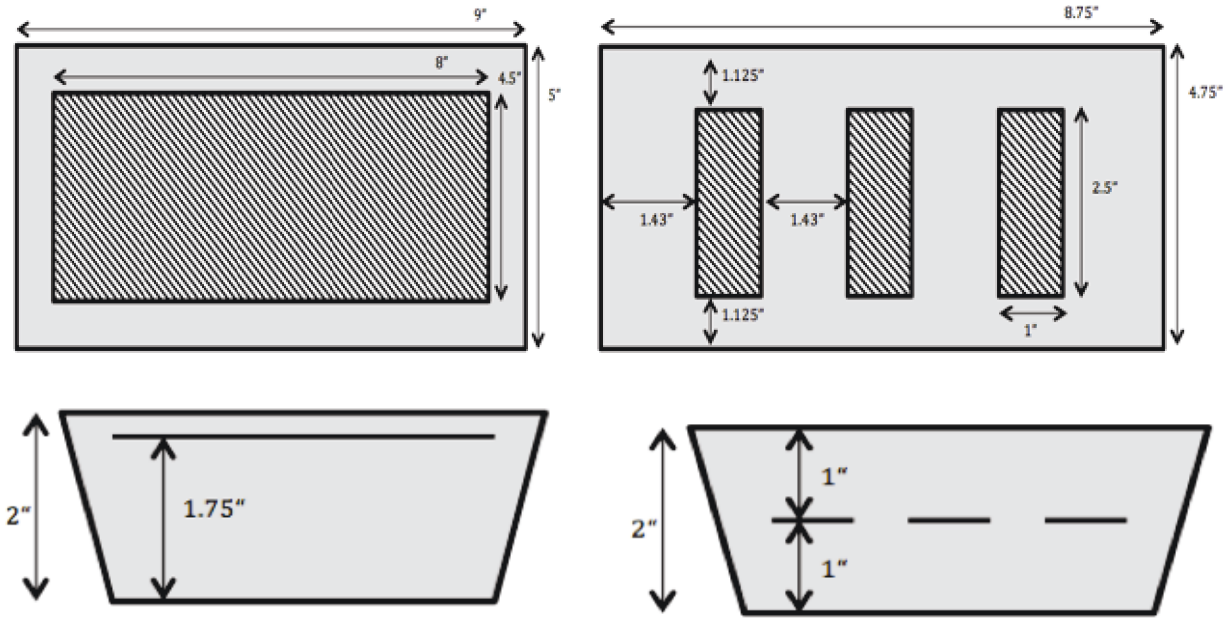

Figure 20. Sketch showing placement of glass in Samples B (left) and C (right).

Figure 20 shows the location of glass embedded in Samples B and C. The dimensions of glass are listed in Table 2. The samples were placed in the molds for 24 hours.

Table 2. Dimension of glass inserts used in the samples.

Thickness	Size
1/16 in.	1 in. × 2.5 in.
1/8 in.	1 in. × 2.5 in.
	8 in. × 4.5 in.
3/16 in.	1 in. × 2.5 in.

5.2 Curing the Samples

After 24 hours, the samples were removed from the molds and cured for the next 24 hours in water at room temperature. After the initial curing, the two sets of samples were cured under different conditions. The first set consisted of Samples A1, B1, and C1, was cured in water at room temperature. Formation of ASR gel under natural ambient conditions is a long-term process. To accelerate ASR gel formation, a second sample set consisting of Samples A2, B2, and C2 was cured in one normal NaOH solution at 80°C, following ASTM C1293 (2008).

Exposure to NaOH increases the alkali content of the environment. This highly alkaline cement reacts with silica from glass to form calcium silicate hydrate gel known as ASR gel. Water cured samples act as the baseline measurement for detection of ASR gel in second set of samples. Table 3 summarizes the composition and curing conditions.

Table 3. Curing conditions of the samples.

Sample	Composition	Curing Condition
A1	Cement only	Water at room temperature
A2		NaOH solution at 80°C
B1	Cement with one glass plate near the top	Water at room temperature
B2		NaOH solution at 80°C
C1	Cement with three glass slides in the middle	Water at room temperature
C2		NaOH solution at 80°C

5.3 Detection of Glass Gel

After curing for two weeks in respective curing conditions, the samples were taken out from the curing environment. NaOH-cured samples are shown in Figure 21. Visual inspection and infrared thermography were performed on the two samples sets.

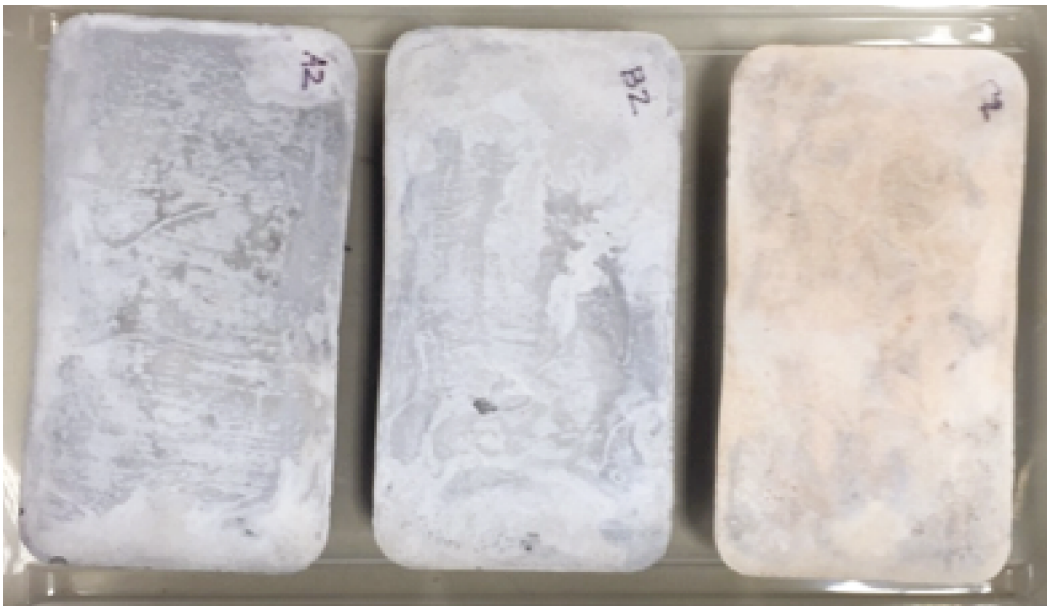

Figure 21. Samples after 14 days of curing in NaOH solution.

5.3.1 Visual Inspection

A visual inspection of the samples was performed. In water cured Samples A1, B1, and C1 no unusual feature was observed. As expected in the absence of glass, Sample A2 also had no abnormal features. In Sample B2, some cracks near the top surface at the location of embedded glass piece were observed and a white powdery effluence was also noticed (see Figure 22). Chemical analysis of the effluence indicated the presence of calcium and sodium. This confirmed the formation of gel (similar to ASR gel) (i.e., calcium silicate hydrate, in Sample B2). Similarly, Sample C2 had smaller glass pieces with large cement cover around them, and effluence was not observed on the sample surfaces.

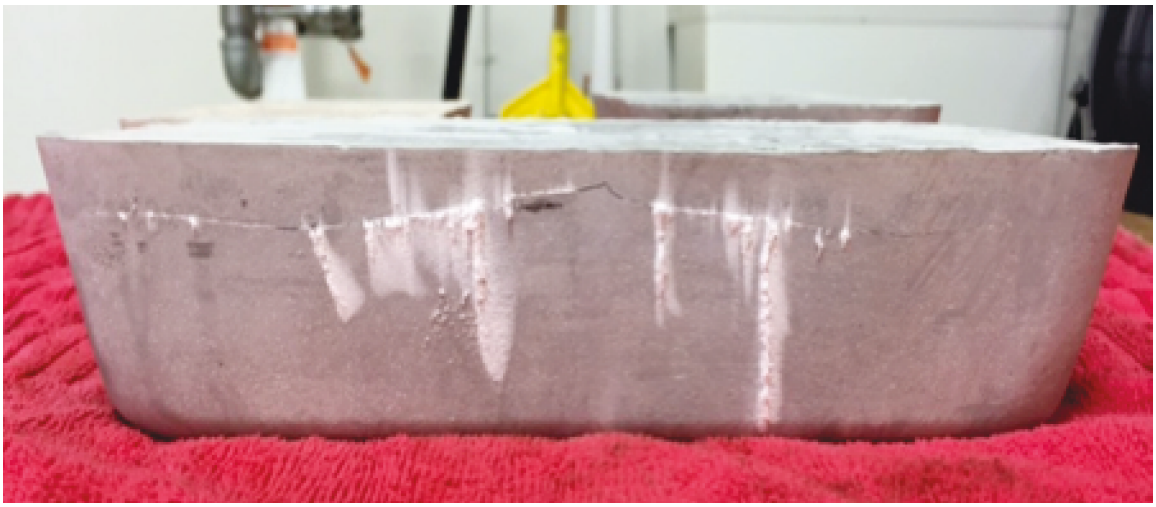

Figure 22. Cracks and gel products seen in Sample B2.

5.3.2 Data Analytics of the Samples

Infrared thermography was conducted on the samples. Heat was applied at the bottom of the samples through a thermal blanket and thermal images were collected on the top surface with a FLIR® infra-red

camera. Figure 23 shows the set-up of the experiment at the Laboratory for Systems Integrity and Reliability at Vanderbilt University. Heat profile applied to the samples is shown in Figure 24.

The following image processing procedures were applied to the thermographic images:

- Cropping
- Smoothing
- Feature calculation and decision-making.

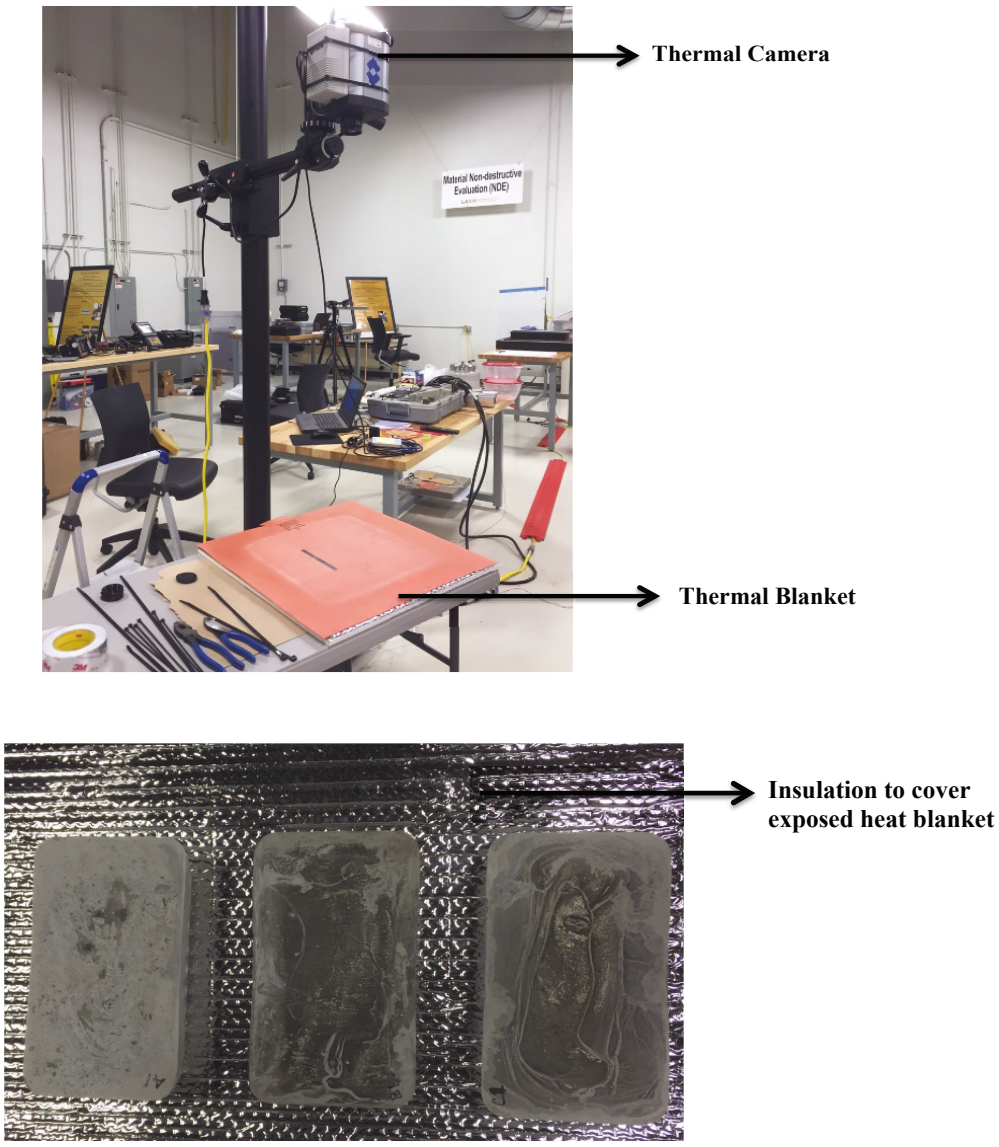

Figure 23. An experimental set-up showing infrared camera and concrete sample (top) and water cured samples placed on the thermal blanket (bottom).

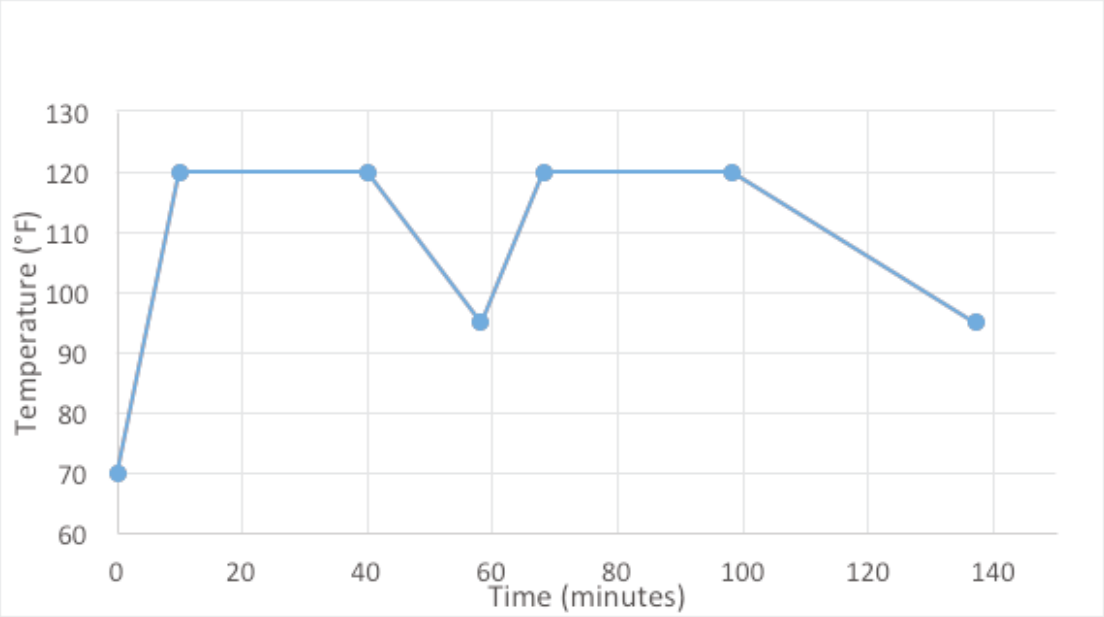

Figure 24. Temperature profile applied to the concrete slab.

5.3.3 Cropping

The thermal images were taken every two minutes for the entire heating and cooling profile described above. The size of the original image taken using the FLIR® infrared camera is 512 × 640 pixels. The three slabs were placed on the thermal blanket and the remaining portion of the blanket was covered with insulation. For clarity in analyzing the temperature profile in the three slabs, the images were cropped. The resulting images are Figures 25 and 26. The cropped size of each slab is approximately 4.05-in.-wide × 7.81-in.-long.

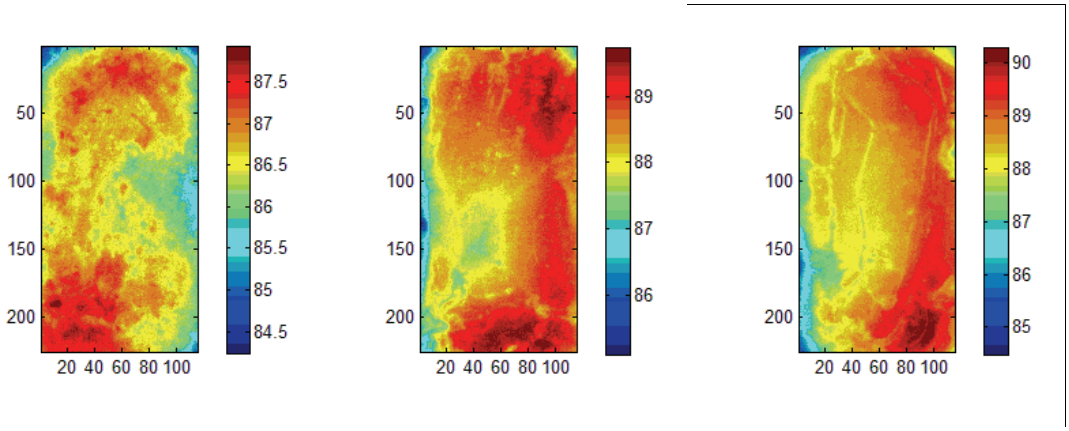

Figure 25. Cropped images for water-cured Slabs A1 (left), B1 (middle), and C1 (right). The images are in pixels and the temperature in Fahrenheit.

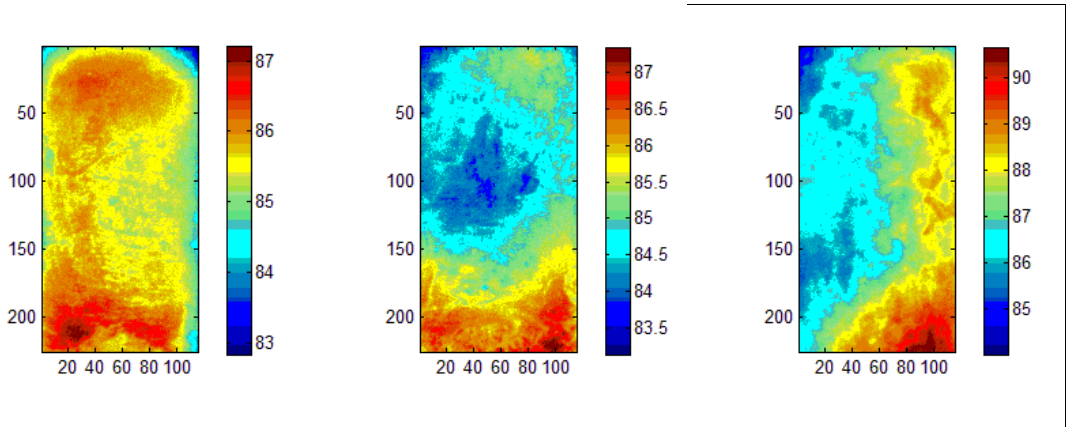

Figure 26. Cropped images for NaOH-cured Slabs A2 (left), B2 (middle), and C2 (right). The images are in pixels and the temperature in Fahrenheit.

This cropping process was completed first for each of the thermographic images provided by the experiments, before the subsequent image processing steps were applied. The cropping parameters are slightly different for the two sets of slabs from slight movements between the two-thermography experiments.

5.3.4 Smoothing

Due to operational and experimental imperfection, the image captured has a significant level of noise. Therefore, smoothing is an important step in image processing. Smoothing of information helps to capture the essential information, while reducing noise (or other fine-scale structures) and transient phenomena.

There are several methods for smoothing data. The simple moving average (SMA) method is classical and effective (Farrar and Worden 2012). More complicated smoothing methods also exist, such as Butterworth filter, Kalman filter, etc. (Chou 1963, Akaile 1974). The smoothing method applied in this study is a two-dimensional SMA, which uses the following equation:

$$SMA = \frac{p_M + p_{M-1} + \cdots + p_{M-(n-1)}}{n} \tag{18}$$

where p_i represents each of the values within a moving window. In our two-dimensional cases, the size-n moving window indicates an n by n matrix. The SMA method is quite simple, yet the effect is significant. After a few tests, a window size of $n = 10$ is seen to be satisfactory.

5.3.5 Feature Calculation and Decision-Making

Due to imperfections and non-uniformity, the data from the heating phase of the experiment do not provide clear differences between the three slabs. On the other hand, the cooling phase was found to be more informative. Since the surrounding thermal environment can be treated as stable, the cooling process can be treated as uniform. Therefore, in the following study, time is focused on the interval from 40 minute to 50 minutes, corresponding to the cooling phase.

After trial and error, feature for comparison is selected to be the temperature difference between the water-cured and NaOH-cured slabs at each time stamp. The hypothesis is that the formation of ASR should change the heat conductivity within the slab. Therefore, temperature difference between the water-cured data and NaOH-cured data for Slab A is selected at each time stamp to be the baseline temperature difference. The corresponding temperature differences for Slab B and C are expected to be different from the baseline.

Based on the Slab A baseline, upper and lower bound values (at each time instant) are selected from the temperature difference between water-cured data and NaOH-cured data. If the temperature difference is outside the bounds, then it is treated as indicating a change in heat conductivity; thus, implying the formation of ASR. Otherwise, the difference is treated as normal, which implies no ASR has formed.

There are several ways of selecting upper and lower bound values. Two methods are considered below. In the first approach, we set the upper bound and lower bound values, respectively, as the maximum and minimum values of the temperature difference among all pixels between the water-cured data and NaOH-cured data for Slab A, at each time stamp. In the second approach, larger magnitude of the difference is used at each time stamp for both lower and upper bound. The upper and lower bound values by the two approaches at different times during the cooling phase are shown in the Appendix (Tables 4 and 5, Figures 29 and 30).

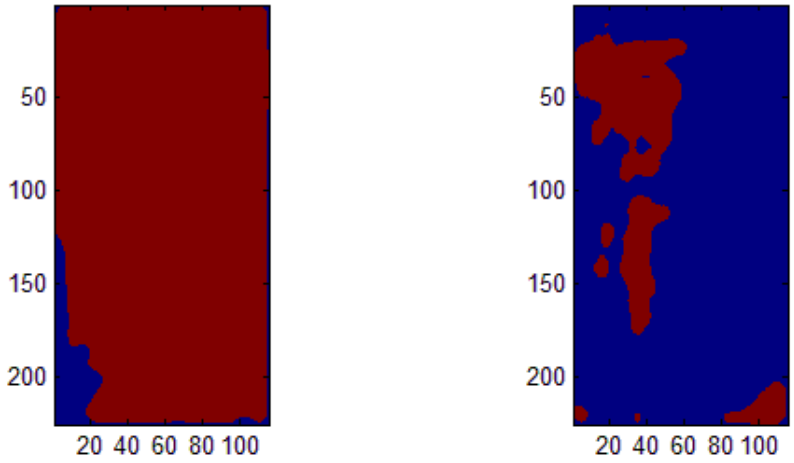

Figure 27. Suspected ASR formation (zone shown in red) for Slab B2 (left) and Slab C2 (right) using the first approach to set the upper and lower bound values (images are in pixels).

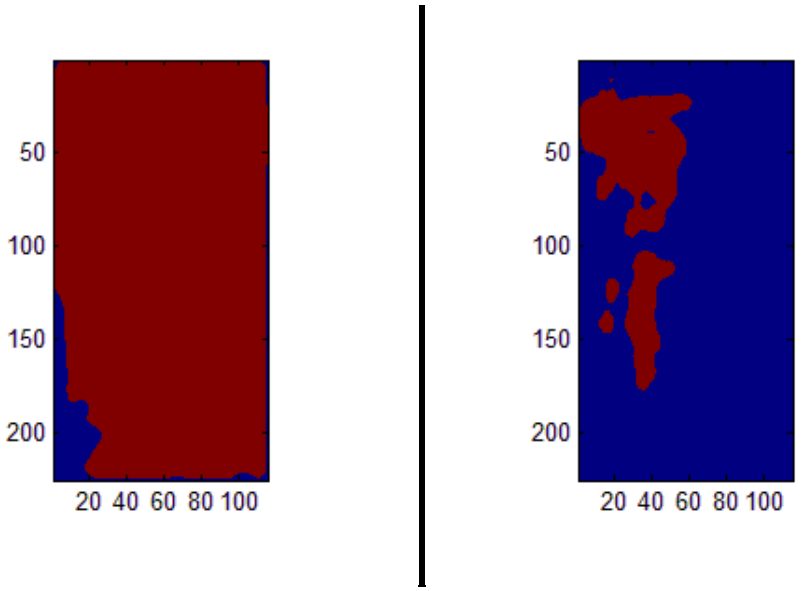

Figure 28. Suspected ASR formation (zone shown in red) for Slab B2 (left) and Slab C2 (right) using the second approach to set the upper and lower bound values (images are in pixels).

Table 4. Upper and lower bound values using the first approach during the cooling process.

Time	40 min	42 min	44 min	46 min	48 min
Upper Bound	0	0	0.0059	0.0059	0.2096
Lower Bound	-1.7218	-1.9336	-1.9074	-2.0686	-1.9473

Table 5. Upper and lower bound values using the second approach during the cooling process.

Time	40 min	42 min	44 min	46 min	48 min
Upper Bound	1.7218	1.9336	1.9074	2.0686	1.9473
Lower Bound	-1.7218	-1.9336	-1.9074	-2.0686	-1.9473

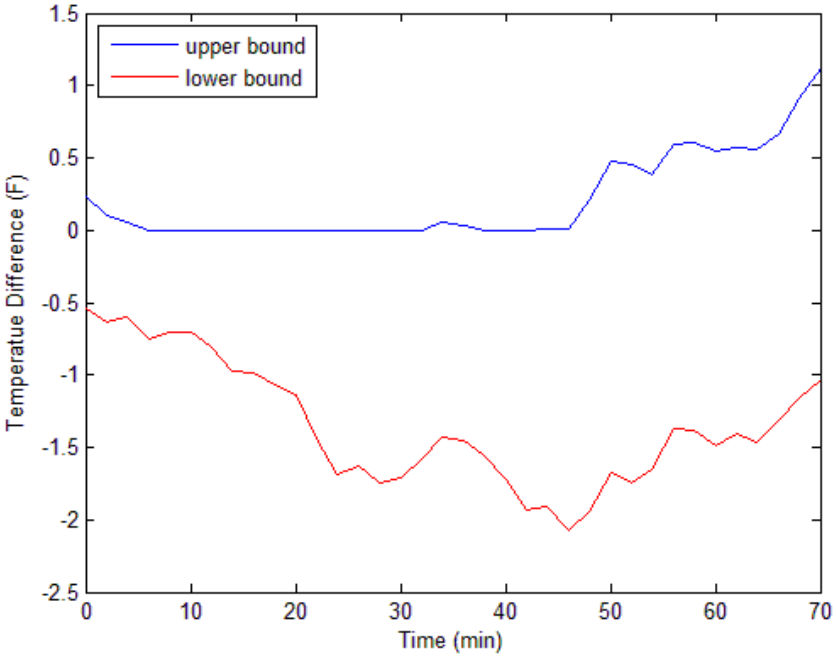

Figure 29. The upper and lower bound values using the first approach.

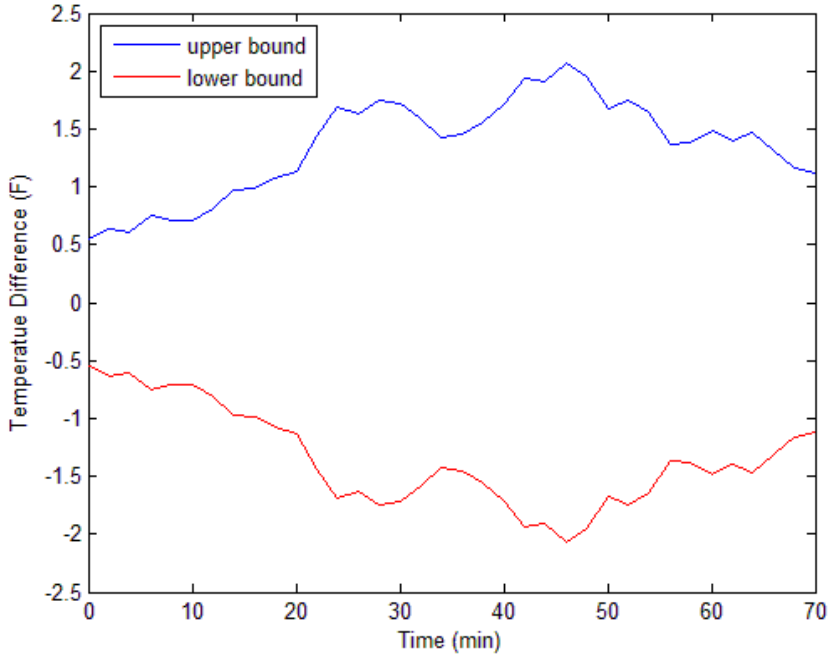

Figure 30. The upper and lower bound values using the second approach.

6. CONCLUSION AND FUTURE PLANS

This report summarized the activities from April to September of fiscal year 2015. These activities are related to concrete structure modeling, monitoring, and diagnosis of ASR in small sized samples. Several mathematical models have been developed and discussed in the literature to capture the characteristics of ASR expansion. A fully thermo-hydro-mechanical-chemical model for ASR based on Ulm et al. (2000) model by Saouma and Perotti (2006) was discussed in this report. The Saouma and Perotti (2006) model considered the effects of stress on the reaction kinetics and anisotropic volumetric expansion induced by ASR. This model was implemented as a GRIZZLY code in the MOOSE framework and was validated using the experimental data from Multon (2003). The results indicated that the model in GRIZZLY was suitable for both isotropic and anisotropic ASR expansion.

The implemented model in the GRIZZLY code was randomly used to initiate ASR in a two- and three-dimensional lattice to study the percolation aspects of concrete. Percolation theory plays an important role in interpreting and understanding the microstructure of cement-based material. The percolation aspects helped determine the transport properties of the material and therefore the durability and service life of concrete. These transport properties are function of percolation threshold.

In a parallel activity, Vanderbilt University developed small sized concrete samples with embedded glass (basically silica), has a strong ability to form ASR and provided a quick proof-of-concept for the proposed SHM framework. The silica in glass reacts with the calcium in cement to form calcium silicate hydride (ASR gel) in the presence of sodium hydroxide. Two sets of three samples each sized 9 in. × 5 in. × 2 in. were cast. For better test sample control, aggregates were replaced by glass (approximately 75% silicon dioxide) in these experiments. By performing data analysis of thermal images, the deformation of glass under thermal loading profile was studied.

In the next phase of the research, Vanderbilt University in collaboration with Professor Eric Giannini of University of Alabama will be working on developing medium sized concrete samples (2 ft × 2 ft × 6 in.) using reactive aggregates with and without steel reinforcement. Full field imaging techniques will be applied to detect ASR expansion in the medium sized sample. A strong theoretical basis will be established and validated to support the proposed monitoring techniques. A data analytics and visualization framework will be developed to analyze and visualize heterogeneous data on a unified and easy-to-use visualization platform. Diagnostic uncertainty quantification will also be formed.

In fiscal year 2016, a collaborative research effort will be performed between the Advanced Instrumentation, Information, and Control and Material Aging and Degradation pathways under the LWRS Program to support large concrete sample instrumentation, data analysis, and uncertainty quantification elements of the SHM framework.

7. REFERENCES

Agarwal, V., and S. Mahadevan, 2014, "Concrete Structural Health Monitoring in Nuclear Power Plants," *Office of Nuclear Energy Sensors and Instrumentation Newsletter*, September 2014.

Christensen, J. A., 1990, "NPAR Approach to Controlling Aging in Nuclear Power Plants," *Proceedings of the 17th Water Reactor Safety Information Meeting, Washington, D.C., 1990,* NUREG/CP-0105, Vol. 3, pp. 509–529.

ASTM C1293 - 08b, 2008, "Determination of length change of concrete due to alkali-silica reaction," ASTM International, West Conshohocken, PA.

AASHTO, 2001, "Guide Specification for Portland Cement Concrete Resistant to Excessive ExpansionCaused by Alkali-Silica Reaction," American Association of State Highway and Transportation Officials.

Akaike, H., 1974, "A new look at the statistical model identification," *IEEE Trans. on Autom Control*, Vol. 19, No. 6, pp. 716–723.

Bak, P., Tang, C., and Wiesenfeld, K., 1987, "Self-organized criticality: an explanation of 1/f noise," *Physical Review Letters*, Vol. 59, No. 4, pp. 381–384.

Bak, P., and Paczuski, M., 1995, "Complexity, contingency, and criticality," *Proc Natl Acad Sci U S A*, Vol. 92, No. 15, pp. 6689–6696.

Chou, Y., 1963, *Statistical analysis, 1st ed*., Canada: Holt, Rinehart & Winston, 1963.

Diamond, S., Barneyback, R. S. Jr., and Struble, L. J., 1981, "On the Physics and Chemistry of Alkali-Silica Reactions," Proceedings of the Fifth Conference on Alkali-Aggregate Reaction in Concrete, National Building Research Institute, Pretoria, South Africa, pp. 1–11.

Farage, M., Alves, J., and Fairbairn, E., 2004, "Macroscopic Model of Concrete Subjected to Alkali Aggregate Reaction," *Cement and Concrete Research*, Vol. 34, pp. 495–505.

Farrar, C. R., and Worden, K., 2012, "Structural Health Monitoring: A Machine Learning Perspective," *1st ed.*, Chichester, West Sussex, U.K: Wiley.

Figg, J., 1987, "ASR—Inside Phenomena and Outside Effects (Crack Origin and Pattern)," Concrete Alkali-Aggregate Reactions, Proceedings of the 7th International Conference, edited by Grattan-Bellew, Patrick E., Noyes Publications, Park Ridge, New Jersey, pp. 152–156.

Jones, T. N., and Poole, A. B., 1987, "Alkali-Silica Reaction in Several U. K. Concretes: The Effect of Temperature and Humidity on Expansion, and the Significance of Ettringite Development," in Concrete Alkali-Aggregate Reactions, Proceedings of the 7th International Conference, edited by Grattan-Bellew, Patrick E., Noyes Publications, Park Ridge, New Jersey, pp. 446–450.

Larive, C., 1998, "Apports Combin'es de l'Experimentation et de la Modélisation à la Comprehension del'Alcali-Réaction et de ses Effets Mécaniques," PhD thesis, Thése de Doctorat, Laboratoire Central des Ponts et Chaussées, Paris.

Mather, B., 1975, "New Concern over Alkali-Aggregate Reaction," Joint Technical Paper by National Aggregates Association and National Ready Mixed Concrete Association, NAA Circular No. 122 and NRMCA Publication No. 149, Silver Spring, Maryland.

Multon, S., 2003, "Evaluation Expérimentale et Théorique des Effets Mécaniques de l'Alcali Réaction sur des Structures Modéles," PhD thesis, Université de Marne la Vallée, France.

Mahadevan, S., Agarwal, V., Cai, G., Nath, P., Bao, Y., Brea, J. M., Myrent, N., Koester, D., Adams, D., and Kosson, D., 2015, *A Simple Demonstration of Concrete Structural Health Monitoring Framework*, INL/EXT-15-34729, Idaho National Laboratory, March 2015.

Mahadevan, S., V. Agarwal, K. Neal, D. Kosson, and D. Adams, 2014, *Interim Report on Concrete Degradation Mechanisms and Online Monitoring Techniques*, INL/EXT-14-33134, Idaho National Laboratory, September 2014.

Naus, D., 2007, "Activities in Support of Continuing the Service of Nuclear Power Plant Safety-Related Concrete Structures," *In Infrastructure Systems for Nuclear Energy* (eds T. T. C. Hsu, C.-L. Wu and J.-L. Li), Chichester, UK: John Wiley & Sons, Ltd.

NRMCA, "Guide Specifications for Concrete Subject to Alkali-Silica Reactions," Mid-Atlantic Regional Technical Committee, June 1993.

Perenchio, W. F., Kaufman, I., and Krause, R. J., 1991, "Concrete Repair in a Desert Environment," Concrete International, American Concrete Institute, Farmington Hills, Michigan, pp. 23–26.

Poole, A. B., 1992, "Introduction to Alkali-Aggregate Reaction in Concrete," The Alkali-Silica Reaction in Concrete, edited by Swamy, R.N., Van Nostrand, R., New York, New York.

PCA, 1940, Tests of Concrete Road Materials from California, Major Series 285, Research Reports, Portland Cement Association, Skokie, Illinois, April 1940.

Stanton, T. E., 1940, "Expansion of Concrete Through Reaction Between Cement and Aggregate," *Proceedings, American Society of Civil Engineers*, Vol. 66, New York, pp. 1781–1811.

Stark, D., 1991, "The Moisture Condition of Field Concrete Exhibiting Alkali-Silica Reactivity," ANMET/ACI Second International Conference on Durability of Concrete, SP-126, American Concrete Institute, Farmington Hills, Michigan, pp. 973–987.

Saouma, V. E., and Perotti, L., 2006, "Constitutive Model for Alkali-Aggregate Reactions," *ACI Materials Journal*, pp. 194–202.

Saouma. V. E., 2014, *Numerical modelling of alkali aggregate reaction*. CRC Press Inc, Boca Raton, Florida.

Smalley, R. F., Jr., Turcotte, D. L., and Solla, S. A., 1985, "A renormalization group approach to the stick-slip behavior of faults," *Journal of Geophysical Research*, Vol. 90, No. B2, pp. 1894.

Turcotte, D. L., Smalley, R. F., Jr., and Solla, S. A., 1985, "Collapse of loaded fractal trees," Nature, Vol. 313, No. 6004, pp. 671.

Ulm, F., Coussy, O., Kefei, L., and Larive, C., 2000, "Thermo-Chemo-Mechanics of ASR Expansion in Concrete Structures, *Journal of Engineering Mechanics*, Vol. 126, No. 3, pp. 233–242.

Xu, H., 1987, "On the Alkali Content of Cement in AAR," in Concrete Alkali-Aggregate Reactions, *proceedings of the 7th International Conference*, edited by Grattan-Bellew, Patrick E., Noyes Publications, Park Ridge, New Jersey, pp. 451–455.

Xu Y., and Chung, D. D. L., 2000, "Cement of high specific heat and high thermal conductivity, obtained by using silane and silica fume as admixtures," *Cement and Concrete Research*, pp. 1175–1178.